

Either IOD Leading or ENSO Leading Triggers Extreme Thermohaline Events in the Tropical Central Indian Ocean

Jin Liu

Sun Yat-Sen University

Dongxiao Wang (✉ dxwang@scsio.ac.cn)

South China Sea Institute of Oceanology Chinese Academy of Sciences <https://orcid.org/0000-0002-7782-0387>

Tingting Zu

South China Sea Institute of Oceanology Chinese Academy of Sciences

Ke Huang

South China Sea Institute of Oceanology Chinese Academy of Sciences

Oscar Y. W. Zhang

Sun Yat-Sen University

Research Article

Keywords: Salinity anomalies, surface buoyancy fluxes, ocean dynamics, advection, tropical Indian Ocean

Posted Date: January 20th, 2022

DOI: <https://doi.org/10.21203/rs.3.rs-1238657/v1>

License: © ⓘ This work is licensed under a Creative Commons Attribution 4.0 International License.

[Read Full License](#)

19 **Abstract**

20 Based on the 12-year (2007-2018) salinity data from Array for Real-Time Geostrophic
21 Oceanography (ARGO), significantly positive salinity anomalies are found in the
22 upper layer of the tropical central Indian Ocean (IO) from 2010 boreal autumn to 2011
23 boreal spring and from 2016 boreal autumn to 2017 boreal spring. Wind, precipitation,
24 outgoing longwave radiation (OLR) and ocean currents from satellite and reanalysis
25 data are utilized to analyze the atmospheric, ocean dynamic processes and the salinity
26 budget associated with the high salinity events. The results indicate that surface
27 buoyancy fluxes are not the dominant factor affecting the positive salinity anomalies,
28 while ocean dynamic processes play a more important role. Under the influence of the
29 La Niña and strong negative Indian Ocean Dipole (nIOD) in 2010 and 2016, positive
30 salinity anomalies appear in the eastern IO at the end of 2010 and 2016 due to strong
31 westerlies and positive zonal currents. But because the La Niña in 2010 is stronger
32 than in 2016, the salinity anomalies in 2010 are stronger, and the decline in the
33 following year is stronger and lasts longer, making the salinity anomalies gradually
34 weakened. Therefore, the maximum value of the salinity anomalies in 2011 is in
35 January, while in 2017 the salinity anomalies first decrease and then increase with the
36 largest in March. Salinity budget analyses also show that ocean advection is the main
37 factor leading to the salinity anomaly variations for these two periods. Among them,
38 the changes of the zonal velocity in the zonal advection anomalies have the greatest
39 impact. The zonal advection is positive and the strongest at the end of 2010 and
40 negative in early 2011, but weak positive at the end of 2016. In early 2017 the zonal
41 advection is first negative, then becomes positive and strengthens in spring, so salinity
42 anomalies in 2017 spring is higher than that in 2011. The entrainment effect during
43 10A11S is more significant than 16A17S and the freshwater flux (FWF) has a small
44 and negative effect on positive salinity anomalies for two events. The mutual effects
45 of horizontal advection, FWF and vertical entrainment together lead to high salinity
46 anomalies. The high salinity anomalies reflect the upper-ocean responses to climate
47 events, which may also influence the regional air-sea interactions and large-scale
48 processes.

49 **Keywords:** Salinity anomalies, surface buoyancy fluxes, ocean dynamics, advection,
50 tropical Indian Ocean

51 **1. Introduction**

52 Ocean salinity is an important aspect of the water mass property (Delcroix and
53 Hénin, 1991). It is not only a key indicator of global hydrological cycle (Durack and
54 Wijffels, 2010; Durack *et al.*, 2012; Schmitt, 2008; Schmitt and Blair, 2015; Skliris *et*
55 *al.*, 2014), but also closely related to the ocean dynamics and thermodynamics
56 (Lagerloef, 2002; Rao and Sivakumar, 2003; Ren and Riser, 2009). Salinity affects
57 lots of aspects of ocean stability (Nyadjro *et al.*, 2012; Schiller *et al.*, 1997), dynamic
58 ocean variability (Stammer, 1997; Sun *et al.*, 2015; Thompson *et al.*, 2006) and
59 complicates air-sea interactions (Grunseich *et al.*, 2013; Guan *et al.*, 2014; Horii *et al.*,
60 2016; Simon *et al.*, 2006; Williams *et al.*, 2010). With the development of the Argo
61 project which provides more observations in the global ocean to conduct detailed
62 studies on the water mass and related ocean dynamics, increasing numbers of salinity
63 and temperature profiles have been collected for the upper 2000 m (Gould *et al.*, 2004;
64 Riser *et al.*, 2008; Roemmich and Owens, 2000; Roemmich *et al.*, 2009). These data
65 offer an opportunity to examine the salinity variability and the related ocean dynamics
66 in the Indian Ocean (IO; Jensen, 2003; Masson *et al.*, 2004).

67 The tropical Indian Ocean (TIO) plays a unique role in the global climate system
68 (Sharma *et al.*, 2010; Subrahmanyam *et al.*, 2011). The IO is rich in precipitation and
69 has the most typical monsoon climate among the global ocean. In the equatorial
70 Indian Ocean (EIO), strong westerlies dominate in boreal spring and autumn during
71 the monsoon transition seasons around May and October-November, and drive the
72 eastward surface currents, known as Wyrтки Jets (Wyrтки, 1973; Reppin *et al.*, 1999).
73 These jets trap the momentum from which the zonal winds input into the oceans in the
74 upper 100 m and significantly influence the climate via horizontal heat, salt and mass
75 transportation in the TIO (Murtugudde *et al.*, 2000). Thermocline perturbations in the
76 form of Rossby waves propagating westward from the southeastern TIO are able to
77 influence the mixed layer through enhancing or depressing the entrainment and
78 vertical mixing. These processes further affect salinity and trigger strong air-sea
79 interactions (Du *et al.*, 2009; Xie *et al.*, 2002; Yokoi *et al.*, 2012). In normal, salinity

80 variations affect ocean stratification and air-sea heat flux in the IO, triggering a
81 response in atmospheric circulation, which significantly influence the
82 thermodynamics in the upper layer (Liang *et al.*, 2018; Zeng and Wang, 2017).
83 Moreover, these further lead to sea temperature variations and convection variations,
84 which indirectly influence the intensity and development of the southwest monsoon
85 and have great impacts on the IO and neighboring countries (Yadav *et al.*, 2019;
86 Sharma *et al.*, 2020). Therefore, it is particularly important and necessary to study the
87 salinity variability in the TIO.

88 Due to significant difference in salinity between the Arabian Sea and the Bay of
89 Bengal, the upper layer salinity in the TIO is generally higher in the west and lower in
90 the east. At the range of 20°S-10°S, the Indonesian throughflow (ITF) and the south
91 equatorial current (SEC) transport low salinity water to the western IO. Different
92 mechanisms are found to be responsible for salinity variability at different depth and
93 on different time scales. Surface salinity is largely controlled by surface freshwater
94 flux (FWF), while upper layer salinity is also affected by horizontal advection,
95 vertical entrainment, turbulence of mixing, diffusion and nonlinear effects (Hasson *et*
96 *al.*, 2013, 2014; Martins and Stammer, 2015). Interannual variability of salinity in the
97 TIO is demonstrated to be closely related to the Indian Ocean Dipole (IOD; Grunseich
98 *et al.*, 2011; Zhang *et al.*, 2013; Nyadjro and Subrahmanyam, 2014; Du and Zhang,
99 2015) and El Niño-Southern Oscillation (ENSO; Clarke and Liu, 1994; Meyers, 1996;
100 Wijffels and Meyers, 2004; Feng *et al.*, 2003, 2010), which are the important climate
101 events that affect the coupled air-sea processes in the TIO (Schott *et al.*, 2009; Phillips
102 *et al.*, 2021). Some studies have shown that these two interannual modes have
103 significant impacts on IO dynamics by modulation of Walker circulation. Furthermore,
104 IOD and ENSO events sometimes appear simultaneously (Saji and Yamagata, 2003;
105 Stuecker *et al.*, 2017). For example, positive IOD (pIOD) can co-occur with EI Niño,
106 while negative IOD (nIOD) can co-occur with La Niña (Cai *et al.*, 2009; Gnanaseelan
107 *et al.*, 2012; Hong *et al.*, 2008). In addition, previous studies denoted that salinity
108 variations might also be related to monsoon intensity. Zhang *et al.* (2020) found that
109 the weakening of the monsoon intensity in the northern Arabian Sea from 2014 to

110 2017 led to changes in ocean dynamics, which further resulted in a prolonged high
111 salinity event.

112 Previous studies mainly focused on salinity variability and its relationship with
113 precipitation and ocean processes in the TIO. Kido *et al.* (2019) concluded that
114 positive sea surface salinity (SSS) anomalies in the southeastern TIO were primarily
115 caused by reduction in precipitation and partly by enhanced evaporation due to
116 increased wind speed, while negative SSS anomalies in the central-eastern EIO were
117 generated by zonal advection anomalies induced by anomalous wind stress. On the
118 other hand, subsurface salinity anomalies were almost entirely caused by wind stress
119 effects mediated by ocean dynamical processes. Their results showed that large-scale
120 ocean changes in response to the pIOD-related atmospheric anomalies were the key
121 drivers of the observed salinity anomalies. Zhang *et al.* (2013) found different salinity
122 variations in the EIO under the influence of pIOD and nIOD. The anomalous
123 westward equatorial currents, attributed to anomalous easterlies, led to low salinity
124 anomalies along the equator during the developing and mature phases of the pIOD
125 events (Du and Zhang, 2015; Nyadjro and Subrahmanyam, 2014; Vinayachandran and
126 Nanjundiah, 2009; Zhang *et al.*, 2013). At the same time, intense northwestward
127 currents off Sumatra strengthened the upwelling and westward high salinity advection
128 near 10°S (Thompson *et al.*, 2006). The anomalies during nIOD were opposite to
129 those during pIOD events. In addition, the salinity variations are also significant
130 during the decay phases and the following year of IOD events in the TIO where
131 circulation system plays an important role in maintaining the heat and salt balance of
132 the entire area, including the Wyrki Jets and the SEC (Sun *et al.*, 2019; Zhang *et al.*,
133 2013; Li *et al.*, 2018). ENSO teleconnection also induces anticyclonic (cyclonic)
134 atmospheric circulation anomalies in the TIO when El Niño (La Niña) appears (Xie *et*
135 *al.*, 2002; Wang *et al.*, 2003), such that the evolutions of ENSO are often associated
136 with the development of the IOD. Grunseich *et al.* (2011) analyzed the surface salinity
137 variations of the EIO when different IOD and ENSO phases occurred. The results
138 showed that the development of IOD was affected according to whether El Niño and
139 La Niña occurred, which further led to the salinity variability. The salinity variations

140 observed throughout the EIO are largely explained by the dynamics responsible for
141 dipole events. What's more, they feedback to the climate events-mainly through ocean
142 stratification, barrier layer, temperature inversion, sea temperature and large-scale
143 circulation and so on (Kido and Tozuka, 2017; Bhavani *et al.*, 2017).

144 However, most of the previous studies concerned about the salinity variations
145 under the influence of multiple climate events or the salinity variation processes
146 during the development of a certain climate event. Sun *et al.* (2019) analyzed the
147 evolution of salinity anomaly variations in the southwestern TIO (SWTIO) during
148 2010-2011 and concluded that the salinity variations were mainly affected by a nIOD
149 event. During early 2011, the positive SSS anomalies shifted to the SWTIO through
150 westward current anomalies. At the same time, the upwelling Rossby waves shoaled
151 the thermocline and mixed layer depth, then brought the high salinity water from the
152 subsurface into the surface layer. These processes further intensified the positive SSS
153 anomalies. Du and Zhang (2015) investigated SSS variations in the TIO during July
154 2010-July 2014. During the nIOD events in 2010,2013, and 2014, their conclusions
155 were similar to the analyses on nIOD above, while the processes reversed during the
156 pIOD events in 2011 and 2012. Till now, there are few studies on the interannual
157 anomalies of tropical central IO salinity and the mechanism comparison between two
158 abnormal events of the same type. Therefore, it is very essential to study the
159 mechanism reasons for the different performance of the same type of significantly
160 anomalous salinity events at different periods. This study will also play a great role in
161 predicting salinity variations in the IO under different climate events in the future.

162 Notably, we find that there are significantly positive salinity anomalies in 2017
163 based on the 6-year CTD observation data of the IO spring voyage, then the ARGO
164 gridded data from 2007 to 2018 are also employed to confirm the phenomena (Figure
165 1): extremely high salinity anomalies are found in the tropical central IO from 2010
166 boreal autumn to 2011 boreal spring (hereafter 10A11S; i.e. from September 2010 to
167 May 2011; Figure 1b) and from 2016 boreal autumn to 2017 boreal spring (hereafter
168 16A17S; i.e. from September 2016 to May 2017; Figure 1c). High salinity anomalies
169 relative to the climatology derived from the Argo data during 2007-2018 reach above

170 0.2 psu. According to the diagrams, 70°E-90°E, 10°S-0° (black closed boxes in Figure
171 1) is the main high salinity anomalies area, so the area will be used as the research
172 focus of the article. In addition, while positive salinity anomalies occur, negative
173 temperature anomalies also appear though the location of the significantly negative
174 anomalies are deviated from the significantly positive salinity anomalies (Figures
175 1e-f), they present a reverse relationship at the same time. During 10A11S there are
176 strong positive salinity anomalies and negative temperature anomalies, but they are
177 weaker during 16A17S. There is a good corresponding relationship between salinity
178 and temperature. Hovmöller diagrams of salinity/temperature anomalies along the
179 longitude and latitude indicate a clear positive-negative changing process from 2007
180 to 2018 (Figure 2). We find that the positive salinity anomalies do last for the periods
181 of time during 10A11S and 16A17S (red boxes in Figure 2). There are extremely high
182 salinity anomalies in these two periods with some differences in intensity and location,
183 as are the two significantly negative temperature anomalies (contours in Figure 2).
184 The results above suggest that the salinity anomalies of the former are stronger than
185 the latter, the range of the anomalies are also larger and the time for the salinity
186 anomaly events to reach the maximum is different. However, for the salinity
187 anomalies in the tropical central IO during 10A11S and 16A17S, their spatial
188 characteristics and formation mechanisms are not well studied, and the processes that
189 cause the positive salinity anomalies are still unclear. Since the end of 2010 and the
190 end of 2016 are the development period of nIOD and La Niña, the periods from
191 January to May in 2011 and 2017 are in the recession year of nIOD and La Niña, we
192 will investigate the salinity variations associated with climate events in the tropical
193 central IO during 10A11S and 16A17S.

194 In this study, we combine salinity data from various datasets and other satellite
195 and reanalysis data to analyze the influence of surface buoyancy fluxes and ocean
196 dynamics on salinity anomalies mentioned above. We explore the underlying
197 dynamics of the extremely high salinity anomalies in the tropical central IO during
198 10A11S and 16A17S and further quantitative analyze the mechanisms for the
199 phenomenon by salinity budget equation. The remainder of this study is organized as

200 follows: the data and methods used are described in Section 2. The results are
201 presented in Section 3. Section 3.1 is mainly about spatial characteristics of the
202 extremely high salinity anomalies. Section 3.2 is mainly about the salinity anomaly
203 variations caused by surface buoyancy fluxes and Section 3.3 mainly denotes
204 anomalies caused by ocean dynamics, which are modulated by related large-scale
205 climate events. Section 3.4 indicates the quantitative analyses of the contribution of
206 each item in the salinity budget equation that causes the anomalous salinity variations
207 during 10A11S and 16A17S. In final, Section 4 gives the discussion and presents the
208 summary of the study.

209 **2. Data and Methods**

210 *2.1.Data*

211 In the study, the Scripps Institution of Oceanography gridded monthly Argo
212 products are used to analyze the salinity variability during 2007-2018. The Argo
213 datasets have a horizontal resolution of $1^{\circ}\times 1^{\circ}$ at each standard pressure level. The L3
214 V5.0 Soil Moisture Active Passive (SMAP) SSS produced by NASA's Jet Propulsion
215 Laboratory (Fore *et al.*, 2020) is used. The SMAP SSS data have a spatial resolution
216 of 0.25° and is available from April 2015 to 2018. We also use European Centre for
217 Medium-Range Weather Forecasts (ECMWF) Ocean Reanalysis System 5 (ORAS5)
218 salinity data with a horizontal resolution of $1^{\circ}\times 1^{\circ}$ and a near-surface resolution of 1 m
219 in the vertical during 2007-2018. In addition, we also download the simple ocean data
220 assimilation (SODA) salinity data from 2007 to 2015 for salinity comparison and their
221 resolution are $0.5^{\circ}\times 0.5^{\circ}$. Here, we use another composite SSS level-3 OS debiased
222 products operationally generated by the Centre Aval de Traitement des Données
223 SMOS (Soil Moisture and Ocean Salinity), which is the water mission of European
224 Space Agency (ESA). Their salinity products are the first-of-its-kind spaceborne
225 mission dedicated to this parameter. Surface salinity has been identified as one of the
226 essential climate variables by Global Climate Observing System program. The
227 nominal requirements for SMOS retrieval are to achieve a 0.1 accuracy (in practical

228 salinity scale), over time/space scales of 10-30 days/200 km (Mecklenburg *et al.*,
229 2008; Font *et al.*, 2010).

230 Furthermore, in situ CTD measurements data for the IO voyage in the spring of
231 2014-2019 are also used. The data are mainly analyzed by two sections: across 0°
232 (equator) section between 80°E and 92°E and across 80°E section between 6°S and
233 2°N. Comparing the salinity data of CTD, Argo and ORAS5 in these two sections, the
234 spatial correlation coefficients are mostly greater than 0.5 (figure not shown). Figure 3
235 shows the average salinity change trend of the two sections. They have large
236 correlation coefficients and relatively small root mean square errors (RMSEs), i.e.
237 there are obvious consistencies between these types of data.

238 The Global Precipitation Climatology Project (GPCP) Version 2.3 monthly data
239 with a resolution of 2.5°×2.5° are supported by NOAA Climate Data Record (CDR)
240 Program, which are available since 1979 (Adler *et al.*, 2003; Huffman *et al.*, 2009)
241 and evaporation with a resolution of 1°×1° from the objectively analyzed air-sea heat
242 fluxes (OA Flux; Yu and Weller, 2007) are used to calculate surface FWF. The flux is
243 mapped on to a 1°×1° grid using linear interpolation, which it is by re-gridding the
244 GPCP data onto OA Flux data.

245 In addition, we use the Oceanic General Circulation Model (OGCM; Masumoto
246 *et al.*, 2004; Sasaki *et al.*, 2004) for the Earth Simulator (OFES) model to get the
247 ocean current data. OFES is forced by National Centers for Environmental Prediction
248 (NCEP) winds and has a horizontal resolution of 0.1°×0.1° with 54 vertical levels. It
249 is based on the Modular Ocean Model Version 3 and run with climatological forcing
250 for 50 years. Moreover, NCEP monthly pressure 10-1000 hPa wind fields with a
251 resolution of 2.5°×2.5° are also used to analyze wind anomalies.

252 The IOD is characterized by the dipole mode index (DMI) which is defined as
253 the difference of area-averaged sea surface temperature anomaly (SSTA) between the
254 western (50°E-70°E, 10°S-10°N) and eastern (90°E-110°E, 10°S-0°) TIO (Saji *et al.*,
255 1999). The ENSO is characterized by the Oceanic Niño Index (ONI) which is defined
256 as the area-averaged SSTA in the Niño 3.4 region (120°W-170°W, 5°S-5°N). We use
257 SST anomaly data from NOAA Extended Reconstructed Sea Surface Temperature

258 version 5 (ERSSTv5) with a resolution of $2^{\circ}\times 2^{\circ}$ to calculate ONI and DMI indexes.
259 Then we choose ± 0.5 times the standard deviation as their thresholds.

260 Except for the general features of salinity, all the anomalous data in the study are
261 obtained by subtracting the climatological annual cycles from the monthly time series
262 during 2007-2018. Most data are all monthly means and downloaded from the
263 Asia-Pacific Data-Research Center of the International Pacific Research Center at the
264 University of Hawaii (<http://apdrc.soest.hawaii.edu>).

265 *2.2.Data validation*

266 To validate the accuracy of the salinity data, we make a comparison between the
267 Argo, ECMWF ORAS5, SMAP and SODA salinity datasets from 2007 to 2018. The
268 spatial distributions of these salinity are similar (figure not shown): the salinity is
269 higher in the west than in the east and gradually decreases from northwest to southeast.
270 To quantify the comparison, we derive the spatial average salinity anomalies for time
271 series analysis (Figure 4) and spatial distributions of salinity RMSEs between Argo
272 data and other salinity data (Figure 5). The Argo salinity anomalies area-averaged
273 compare well with that for ECMWF ORAS5, the SODA and SMAP data. Their
274 curves are very close (Figure 4). The area-averaged correlation coefficients and
275 RMSEs between the Argo and SMAP are respectively 0.9654 and 0.1181 psu,
276 between the Argo and ECMWF ORAS5 are respectively 0.9879 and 0.0362 psu and
277 between the Argo and SODA are respectively 0.9817 and 0.0376 psu. We can also
278 find that the salinity RMSEs between Argo and other data are relatively small in the
279 IO (Figure 5), especially in the main high salinity anomalies area (see black boxes in
280 Figure 1), indicating the reliability of the Argo data. In general, all comparisons
281 indicate good agreement between the Argo salinity and other datasets. And the two
282 data of Argo and ECMWF ORAS5 have the highest similarity and the smallest RMSE
283 so later we will use ECMWF ORAS5 salinity data to calculate the salinity budget
284 equation.

285 *2.3.Methods*

286 To identify the key processes governing the evolution of salinity anomalies,
 287 salinity budget analysis has been widely used. The salinity budget equation (Gao *et al.*,
 288 2014; Qu *et al.*, 2013) can be written as:

$$\frac{\partial[S]}{\partial t} = -\frac{(P-E)}{h} [S] - \nabla_H (uS, vS) - \frac{1}{h} ([S]-S_{-h}) w_e - \partial_Z (wS) + \varepsilon$$

289 where the square bracket means the depth average within the selected depth. For
 290 instance, $[S]$ means the average salinity above 50 m. $\frac{\partial[S]}{\partial t}$ is the salinity tendency; P
 291 and E are the precipitation and evaporation, h is taken as 50 m; u , v and w are the
 292 zonal, meridional and vertical velocities; and S_{-h} is chosen as the salinity 15 m
 293 below the selected depth base (Ren *et al.*, 2011). The subscript H and Z denote
 294 horizontal and vertical components of the variables, respectively. $\nabla_H = (\frac{\partial}{\partial x}, \frac{\partial}{\partial y})$ and
 295 $\partial_Z = (\frac{\partial}{\partial z})$ represent for the horizontal and vertical gradient operators, respectively. In
 296 the following, the first and second terms of equation on the right-hand side represent
 297 the surface FWF and the horizontal advection, respectively. Horizontal advection is
 298 divided into zonal advection and meridional advection. Vertical entrainment terms
 299 consist of the third and fourth terms on the right-hand side. The research combines the
 300 vertical entrainment terms with horizontal advection and calls it S-adv. The horizontal
 301 and vertical mixing and the accumulation of errors from the other terms are added into
 302 the residual term ε . We nominally consider the salinity and temperature at 10 m (first
 303 level) as that from the sea surface.

304 The entrainment velocity w_e is calculated as $w_e = h (\frac{\partial u}{\partial x} + \frac{\partial v}{\partial y})$. In addition, the
 305 residual term ε is calculated by the salinity tendency minus the sum of FWF and S-adv.
 306 To separate the interannual variability from the seasonal cycle, each variable is
 307 divided into two parts: the climatological mean seasonal cycle and the anomaly
 308 variability separated from the seasonal cycle (e.g., $u = \bar{u} + u'$). Thus, by neglecting
 309 the higher-order nonlinear terms, the salinity horizontal advection term (Zhang *et al.*,
 310 2013) in the above equation can be rewritten as

$$-\nabla_H (uS, vS) = -(\bar{u} \frac{\partial[S]'}{\partial x} + u' \frac{\partial[\bar{S}]}{\partial x} + \bar{v} \frac{\partial[S]'}{\partial y} + v' \frac{\partial[\bar{S}]}{\partial y})$$

311 In the equation, the horizontal advection term contains two parts: One is due to the
312 variability of ocean current (e.g., $-u' \frac{\partial \overline{[S]}}{\partial x}$), the other is due to the variability of
313 salinity gradient (e.g., $-\bar{u} \frac{\partial [S]'}{\partial x}$).

314 **3. Results**

315 *3.1. Spatial characteristics of extremely high salinity anomalies*

316 Figure 6 shows the monthly Argo area-averaged salinity/temperature variations
317 and their anomalies with depth from 2007 to 2018. According to what we have
318 learned before, salinity refers to the frequent low salinity events within the upper 50 m
319 of the entire periods due to the influence of surface FWF. In particular, extremely high
320 salinity anomalies and a depth of approximately above 50 m are clearly identified
321 during 10A11S and 16A17S (Figure 6b). Their intensities and the development trends
322 of salinity anomalies are different. In addition, when positive salinity anomalies occur,
323 significantly negative temperature anomalies also appear (contours in Figure 6b).
324 Normally, we propose that salinity anomalies are mainly within 50 m of the upper
325 layer. Compared with other low salinity events, such extremely high salinity
326 anomalies during these two periods are uncommon. Furthermore, strong temporal
327 correspondence between life cycle of salinization events in these two periods clearly
328 indicates the dominance of these events on interannual variability of salinity in the
329 tropical central IO. It is worth mentioned here that out of 12 years of study (figure not
330 shown), only these two periods show abnormally strong salinization events. Hence,
331 we mainly focus on these two extremely high salinity anomalies in the tropical central
332 IO and the factors responsible for their formations.

333 Concerning about the spatial distributions of three-month moving mean
334 extremely high salinity anomalies in the main high salinity anomalies area (see black
335 boxes in Figure 1) during 10A11S and 16A17S (shading in Figure 7), the high value
336 centers are different among all periods. In 10A11S (Figures 7a-c), the positively high
337 salinity anomalies first appear in the eastern IO, then gradually become stronger, and
338 finally decrease, with the strongest in January. While in 16A17S (Figures 7d-f), the

339 positive salinity anomalies are relatively small first, then gradually become larger
340 with the strongest in March. Comparing two events during 10A11S and 16A17S, the
341 salinity anomalies in former have a more obvious tendency to move westward and
342 southward. The latter tends to extend eastward in the later period. Obviously the
343 intensity of the former event is greater than that of the latter from September to
344 February, but the latter is slightly stronger in March-May.

345 Based on previous studies, the salinity anomaly variations are mainly related to
346 two factors: surface buoyancy fluxes and ocean dynamics. Among them, the ocean
347 dynamic processes are mainly caused by the climate modes, such as IOD and ENSO.
348 Figure 8 gives the time series of the ONI and DMI indexes and the correlation
349 coefficients between ONI/DMI and salinity anomalies during 2007-2018. We can find
350 that salinity anomalies in the research area are negatively correlated with ENSO and
351 IOD, and the correlation coefficients reach the maximum when the salinity anomalies
352 lag ENSO by 3 months and IOD by 4 months, which are -0.4178 and -0.4610,
353 respectively. Furthermore, the development processes of climate events in 2010-2011
354 and 2016-2017 are different. 2010 is a strong La Niña year, which reaches maturity at
355 the end of 2010 and begins to decline in 2011. In contrast, 2016 is a weaker La Niña
356 year, basically close to normal. For IOD events, both 2010 and 2016 are strong nIOD
357 years, but the nIOD in 2016 lasts longer. And in the first half of 2017, it shows a
358 weaker pIOD. But weak pIOD only appears in the second half of 2011. To sum up, the
359 La Niña in 2016 is much weaker than in 2010, but IOD events in 2016-2017 is little
360 stronger than that in 2010-2011. According to the negative correlation coefficients
361 between ENSO/IOD and salinity anomalies, there may be positive salinity anomalies
362 caused by co-occurrence of IOD and La Niña during 10A11S and 16A17S. Later, we
363 will focus on analyzing how climate models affect the salinity anomaly variations.

364 From the discussions above, two obvious positive salinity anomalies can be
365 found during 10A11S and 16A17S. The development processes and intensities of the
366 two anomalies are different and they may all be influenced by surface buoyancy
367 fluxes and ocean dynamic processes. Next, we separately analyze the impact and
368 contributions of these two factors on the salinity anomalies in the tropical central IO

369 during 10A11S and 16A17S.

370 *3.2. Salinity anomaly variations caused by surface buoyancy fluxes*

371 From the analyses above, there are significantly high salinity anomalies during
372 10A11S and 16A17S. We first analyze the positive salinity anomaly variations caused
373 by the surface buoyancy fluxes in the main high salinity anomalies area during
374 10A11S and 16A17S.

375 Figure 9 shows the spatial distributions of cumulative precipitation anomaly and
376 surface FWF in three months during 10A11S and 16A17S. There are two obviously
377 and anomalously high precipitation centers in 2010 autumn (contours in Figure 9a)
378 and 2017 spring (contours in Figure 9f), indicating that the precipitation is large for
379 these two periods and small for other times. Moreover, the locations of large
380 precipitation are mainly east of 82°E. So, there is more precipitation in 2010 autumn
381 than 2016 autumn and in 2017 spring than 2011 spring. Furthermore, the abnormal
382 values of evaporation during 10A11S and 16A17S are small and the difference in
383 evaporation between the two periods is also very small (figure not shown). The net
384 surface FWF (shading in Figure 9) obtained by subtracting precipitation from
385 evaporation is roughly the opposite of precipitation anomaly distributions. In other
386 words, the net surface FWF in 2010 autumn is smaller than 2016 and in 2017 spring is
387 smaller than 2011, which these two periods have more significantly negative values.
388 According to the previous analyses, the area is also a corresponding high salinity
389 anomalies area, the salinity anomalies during 10A11S (see Figures 7a-c) first increase,
390 then decrease gradually and the strongest is in January. The salinity anomalies during
391 16A17S (see Figures 7d-f) first increase, then decrease and finally increase, with the
392 strongest in March. The salinity anomalies in 2010 autumn are higher than 2016
393 autumn and in 2017 spring are higher than that 2011 spring. But the FWF in 2010
394 autumn is also stronger than that in 2016 autumn and in 2017 spring is stronger than
395 that 2011 spring. The FWF variations in these two periods are not corresponding to
396 the salinity anomalies during the same period. Therefore, FWF does not make a
397 significant contribution to salinity variations. The above analyses show that the high

398 salinity anomalies cannot be explained by FWF, so the extremely high salinity
399 anomalies are not only determined by the surface buoyancy fluxes and they have a
400 small effect, but also by other ocean dynamic processes.

401 According to the positive salinity anomalies corresponding to the negative
402 temperature anomalies, it is further inferred that during 10A11S, there is no obvious
403 upwelling at the beginning in the tropical central IO area, so it is beneficial to
404 maintain higher temperature in the upper layer, promoting the occurrence of
405 convection, and further lead to increase in precipitation (Figure 9a). In the later stage,
406 the situation is reversed. Similarly, the situations during 16A17S show that the
407 precipitation is small first, and later precipitation becomes large due to the convection
408 processes caused by SSTA (Figure 9f). Normally, because the precipitation in 2010
409 autumn and 2017 spring is larger than that the corresponding period in 2011 and 2016,
410 it should cause the positive salinity anomalies in the former periods to be smaller than
411 that in the latter periods, but in fact it's the opposite. Therefore, the above results
412 indicate that the main reason of the positive salinity anomalies is not surface
413 buoyancy fluxes. Another factor should be responsible for the salinity anomalies in
414 the tropical central IO. Ocean dynamic processes may contribute more to the
415 extremely high salinity anomalies. Next, our studies focus on the impacts of ocean
416 dynamics on extremely high salinity anomalies in the tropical central IO for these two
417 periods.

418 *3.3. Salinity anomaly variations caused by ocean dynamics*

419 We have analyzed surface buoyancy fluxes and initially conclude that it is not the
420 main cause of the extremely high salinity anomalies. As mentioned above, the ocean
421 dynamic processes that cause salinity variations may be related to large-scale dynamic
422 processes such as IOD and ENSO (see Figure 8). Then, let's analyze how the climate
423 modes modulate the ocean dynamic processes, which in turn affect the salinity
424 anomalies.

425 Figure 10 and 11 show the evolution of monthly mean salinity anomalies and the
426 related processes during 10A11S and 16A17S, respectively. During

427 September-November (Figures 10a-c and 11a-c), the zonal wind anomalies in the EIO
428 is positive, indicating that there are abnormal westerlies at this time. And the
429 anomalies in 2010 are stronger than that in 2016. According to the previous analysis,
430 2010 and 2016 are nIOD and La Niña years. La Niña in the tropical Pacific leads to an
431 increase in the Walker circulation and the effect of atmospheric bridges also increases
432 the Walker circulation in the TIO. Therefore, for the strong La Niña year in 2010, the
433 counterclockwise circulation in the TIO has strengthened, and there are stronger
434 westerly anomalies. During the same period of 2016, it is mainly the process of
435 changing from the southwesterlies to the westerlies, which result in stronger eastward
436 currents in 2010 than in 2016 and further lead to the intrusion of high salinity water
437 from the west to the east in the TIO. Thus, under the influence of strong westerlies
438 and eastward currents, the salinity anomalies in September-November 2010 are higher
439 than the corresponding months in 2016. It can be seen from the contours in Figures
440 10b-c that the high salinity anomalies in 2010 can reach the coast of Sumatra Island in
441 the eastern IO and above 0.4 psu. This is related to the facts mentioned earlier (see
442 Figure 8), the La Niña in 2010 is much stronger than in 2016 and the intensities of
443 nIOD are similar in two years. Hence through the co-occurrence of stronger La Niña
444 and nIOD in 2010, Walker circulation becomes stronger and leads to stronger
445 westerlies, which in turn result in stronger eastward currents, then these currents
446 further cause extremely high salinity anomalies in the central-eastern TIO. However,
447 through the co-occurrence of much weaker La Niña and nIOD in 2016, weak Walker
448 circulation causes weak eastward currents and positively low salinity anomalies in the
449 central-eastern TIO. According to previous studies, during nIOD and La Niña years,
450 the anomalous westerlies diverge to the south off the south Java-Lesser Sunda coast.
451 The positive wind stress curls trigger anomalous cyclonic circulation in the
452 southeastern IO and forced upwelling Rossby waves to slowly propagate westward.
453 Evidently, it is more significant in 2010 than in 2016.

454 During December-February of the following year, the central-eastern EIO zonal
455 wind anomalies weaken (Figures 10d-f and 11d-f). So as the westerly anomalies
456 weaken and it is mainly the process of changing from the westerlies to the

457 northwesterlies, the eastward currents near the equator also weaken and even the
458 eastward currents turn into westward currents. They are more obvious in 2011. As a
459 result, affected by the extremely high salinity anomalies in the eastern IO caused by
460 the eastward currents under the combined action of strong La Niña and nIOD in the
461 early stage, the high salinity water is transported westward, which leads to the high
462 salinity anomalies in the tropical central IO. From the high salinity anomalies center
463 (contours in Figures 10d-f) we can see the trends of high salinity anomalies gradually
464 moving westward. In 2017, affected by the weak positive salinity anomalies in the
465 eastern IO caused by the weaker eastward currents under the combined action of weak
466 La Niña and nIOD in the early stage and now weaker westward currents, the high
467 salinity anomalies do not move significantly westward. These phenomena are mainly
468 caused by the weakening of La Niña and nIOD events of different intensities. At the
469 same time, the eastward Kelvin waves generated by the westerlies in October reach
470 the east coast and reflect to form westward propagating upwelling Rossby waves. Due
471 to the influence of upwelling Rossby waves, the lower layer of higher salinity water is
472 transported upwards, which has a positive contribution to the salinity anomalies.
473 Because the La Niña was stronger in 2010 than in 2016, the high salinity in former
474 caused by vertical entrainment at this time is also stronger than the latter. Thus, the
475 salinity anomalies begin to gradually decrease due to the decline of climate events and
476 the salinity anomalies in these three months of 2011 are higher than that of 2017.

477 During March-May, La Niña in 2011 is still in a recession. The easterly
478 anomalies are mainly on the equator in 2011, especially from April to May, while in
479 2017 there are obvious westerly anomalies. So, in 2011(Figures 10g-i) there are still
480 westward currents and the upwelling Rossby waves caused by the previous period
481 continue to move westward, which cause the positive salinity anomalies to gradually
482 move westward and southward. And the positive salinity anomalies decrease in the
483 tropical central IO. In 2017 (Figures 11g-i), due to the weak La Niña in 2016, ENSO
484 has gradually become normal during this period. The easterlies become westerlies and
485 they are clearly stronger in April. The westward currents turn into eastward currents,
486 which result in positive salinity anomalies in the tropical central IO. Therefore, at this

487 time the positive salinity anomalies in 2017 are stronger than in 2011.

488 IOD may modulate the equatorial winds and then affects the related wave
489 processing. It also shows direct influence on the high salinity events. According to
490 previous researches (Izumo *et al.*, 2008; Yokoi *et al.*, 2008), Seychelles Dome (SD;
491 60°E-80°E, 10°S-5°S) is a remarkable oceanic thermal dome along monsoon and
492 southeasterlies. Due to its unique location, which is under the joint control of
493 monsoon and southeasterlies, SD has a semi-annual cycle associated with upwelling
494 in the boreal spring. Above the SD, SSTAs are sensitive to variability in the upwelling
495 and these are especially so in their seasonal and interannual variation (Tozuka *et al.*,
496 2010). Yokoi *et al.* (2012) used an ocean general circulation model (OGCM) to
497 analyze seasonal and interannual variations of the SST above the SD. Their results
498 indicated the SSTA in the SD was closely related to IOD. The pIOD (nIOD) might
499 induce the weakened (strengthened) SD. Since 2010 and 2016 are nIOD years, there
500 will be strong SD in 2011 spring and 2017 spring, so there is strong upwelling in the
501 60°E-80°E, 10°S-5°S that causes cold and salty water in the lower layer to be
502 transported upward. In 2011 spring, high salinity water caused by upwelling will
503 move towards the western IO under the influence of the westward currents. While in
504 2017 spring, the strong eastward currents cause the high salinity water to move
505 eastward, which have contributions to the positively high salinity anomalies in the
506 tropical central IO.

507 Between the two extremely high salinity anomaly events analyzed (i.e.
508 2012-2016; see Figure 2), there are significantly negative salinity anomalies, which
509 are in a freshening stage, especially from 2011 autumn to 2013 spring (hereafter
510 11A13S) and from 2015 autumn to 2016 summer (hereafter 15A16S) are the most
511 obvious. According to Figure 8, 2011 is a weak pIOD year with weak La Niña and
512 2012 is a strong pIOD year without El Niño or La Niña, while 2015 is a strong pIOD
513 year with strong El Niño. By comparison, the previous significantly negatively low
514 salinity event occurs in pIOD year without strong El Niño and the latter occurs in a
515 strong El Niño and pIOD year. Through analyzing the salinity anomalies and related
516 processes during 15A16S in Figure 12, it is just the opposite of 2010-2011 analyzed

517 previously (see Figure 10). On the one hand, under the influence of strong pIOD at the
518 end of 2015, the westward currents caused by the abnormal easterlies result in
519 significantly negative salinity anomalies in the central-eastern IO (contours in Figure
520 12). Moreover, when El Niño occurs, the Walker circulation weakens, leading to a
521 weakening of the clockwise circulation formed under the influence of pIOD. It further
522 causes abnormal salinity weakening, but its impact is relatively small compared to
523 pIOD. On the other hand, the negative wind stress curls in the southeastern IO trigger
524 anticyclonic circulation, which lead to the downwelling Rossby waves to propagate
525 westward. Similarly, the same phenomenon occurs during 11A13S (figure not shown).
526 The IOD intensities for 11A13S and 15A16S are similar, but no El Niño occurred
527 during 11A13S, so the salinity anomalies caused by the above are stronger than
528 15A16S. Therefore, the salinity of the central-eastern TIO also shows significantly
529 negative anomalies in some years, indicating a major influence of climate events on
530 salinity anomalies, highly consistent with the positive salinity anomalies in 2010-2011
531 and 2016-2017 by the analyses above.

532 Besides, weak positive salinity anomalies are found in the autumn of 2013 (see
533 Figure 2), which do not fully develop and disappear soon. Looking at Figure 8, we
534 find that 2013 is a weaker nIOD year than the intensities of nIOD in 2010 and 2016,
535 and there is no El Niño or La Niña. Under such ocean dynamic condition, the
536 abnormal westerlies caused by nIOD are very weak, leading to weak eastward
537 currents, so the positive salinity anomalies are very small and quickly decline.
538 Generally speaking, the periods from 2012 to 2016 are mainly the stage of salinity
539 freshening. In 2010, nIOD causes positive salinity anomalies in the tropical central IO
540 during 10A11S, pIOD in 2011 and 2012 causes negative salinity anomalies in the
541 tropical central IO during 11A13S. pIOD in 2015 leads to negative salinity anomalies
542 during 15A16S and nIOD in 2016 leads to positive salinity anomalies during 16A17S
543 in the tropical central IO.

544 In addition, La Niña event as strong as 2010 that occurs during 2007 without an
545 nIOD event does not produce any significantly positive salinity anomaly in 2007-2008
546 (see Figure 8). Further based on the above results, we also analyze the relationships

547 between the salinity anomalies in the tropical central IO from 1979 to 2018 based on
548 ECMWF ORAS5 data and IOD/ENSO. Comparing 1998, 2010 and 2016: 1998 and
549 2010 have similar La Niña intensities, but in 2010 the nIOD is stronger, and the
550 resulting salinity is abnormally stronger; While the La Niña intensity in 2016 is
551 significantly weaker than 1998, but the nIOD intensity is stronger, resulting in
552 abnormally stronger salinity in 2016-2017. Comparing 1997, 2015 with 1994, 2006:
553 strong El Niño occurred in the first two years and weak El Niño occurred in the
554 second two years, but the negative salinity anomalies in former are weaker than the
555 latter; And comparing 1982 with 2015: both two years have similar pIOD intensities.
556 Among them, a strong El Niño occurs in 1982 and a much stronger El Niño occurs in
557 2015. The salinity anomalies are the opposite of the El Niño strength. In 1982 it
558 causes strong negative salinity anomalies and in 2015 it leads to weak negative
559 salinity anomalies.

560 The above multiple analyses indicate that the interannual variability of oceanic
561 and atmospheric conditions associated with IOD may be playing a crucial role on the
562 modulation of salinity variability in the tropical central IO. ENSO has a certain
563 influence on its anomalous salinity intensity. When IOD events of similar intensity
564 occur, ENSO events of different intensities will cause an abnormal salinity difference.
565 Our results show some resemblance with the finding of Zhang *et al.*, (2013), such as,
566 the interannual variability of salinity in the TIO was primarily controlled by IOD
567 events rather than ENSO events and the opinions of previous studies (Burns and
568 Subrahmanyam, 2016) that IOD events seemed to be the dominant influence on
569 salinity during peak IOD months of co-occurring event years.

570 As a result, with the influence of different intensities of La Niña and nIOD
571 events, the salinity variations and the related processes show different characteristic
572 during 10A11S and 16A17S. Given the typical displacement of the salinity front in
573 the tropical central IO when climate events occur and the typical magnitude of the
574 current anomaly there (about 0.2 m s^{-1}), the 3-4-months delay between salinity
575 variability and DMI/ONI evolution can be simply observed as the advective timescale
576 of the salinity front through the central IO. Because the nIOD events in 2010 and

577 2016 are both strong, significantly positive salinity anomalies first appear in 2010
578 autumn and 2016 autumn and last until the following spring. Due to stronger La Niña
579 event in 2010 than 2016, the high salinity anomalies reach the maximum before La
580 Niña recession, so they reach the maximum in January. While in 2017, La Niña
581 recession quickly returns to normal, so the salinity anomalies first decrease and then
582 increase again due to the influence of wind fields, ocean currents, etc. Thus, the
583 anomaly maximum value is in March.

584 *3.4. Salinity budget analyses of two extremely high salinity events*

585 From the previous analyses, under the influence of different intensities of nIOD
586 and La Niña events, the salinity anomalies and the related processes during 10A11S
587 and 16A17S are quite different in the tropical central IO. Extremely high salinity
588 anomalies may be related to surface buoyancy fluxes and ocean dynamic processes.
589 To further understand the mechanisms associated with the salinity anomaly variations,
590 we carry out the salinity budget analyses to discuss the main processes contributing to
591 the salinity variability. The salinity budget using datasets with uncertainties from
592 different sources has a large residual term. Therefore, we only provide qualitative
593 analysis to understand the relative contributions of the horizontal advection, vertical
594 entrainment and FWF during 10A11S and 16A17S.

595 From the previous analyses, we can conclude that there are obviously high
596 salinity anomalies in the tropical central IO during 10A11S and 16A17S. Figure 13
597 shows the salinity variation tendency and main processes during 10A11S and 16A17S.
598 The value of each term in the salinity budget equation is different in different periods.
599 Some months of these items are larger in former event and other months are larger in
600 latter event. During 10A11S (Figures 13a-c), Salinity increases first, then gradually
601 decreases from December, and finally increases again. At the same time, horizontal
602 advection plus vertical entrainment, which represent ocean dynamic processes (S-adv
603 term in Figure 13a) are positive first, then negative and finally positive. It can be
604 found that S-adv term is the largest term even if the residual item is sometimes large,
605 so it is the main factor for the salinity variations for the periods. There is a larger

606 positive advection term in September-October 2010 and the advection effects result in
607 the salinity to increase faster. In early 2011, the advection term becomes negative,
608 indicating that it has an inhibitory effect on the increase in salinity, so the salinity
609 shows a trend of gradual decrease. Later, due to smaller positive advection, the
610 salinity increased again. Among them, these variations are mainly caused by zonal
611 advection, especially the abnormal changes of the zonal currents. During 16A17S
612 (Figures 13d-e), the salinity changes are very small in the early stage and become
613 large in the later period. The S-adv term changes are the same. Thus, the advection
614 plays a major role in the salinity variations and there are larger values in March-May.
615 In general, advection promotes the increase of salinity, especially the zonal advection.

616 The FWF is all negative, indicating that it has a negative effect on the salinity
617 variations. The influence in 2010 autumn and 2017 spring is more significant but
618 other periods have a little effect on salinity. In the early stage of the event, the S-adv
619 term in 2010 was greater than 2016. But the S-adv term in 2017 spring is much
620 stronger than that in 2011 spring. In early 2011, the S-adv term is strong negative, and
621 then weak positive. While in early 2017, the S-adv term changes from small to large.
622 Thus, the high salinity anomalies are caused by the mutual effects of the advection
623 term and the FWF term, but the contribution of the advection term is greater.

624 In addition, the contributions of the vertical entrainment item are also more
625 obvious and it's larger in 2011 than 2017 (S-advz term in Figure 13b and 13e). Sun *et al.*
626 (2019) suggested that Rossby waves would propagate westward to the southeastern
627 TIO during IOD events. The downwelling Rossby waves are associated with the
628 negative wind stress curls anomalies in the southeastern TIO during pIOD (Xie *et al.*,
629 2002, 2009; Yu and Rienecker, 1999; Yu *et al.*, 2005; Zhang *et al.*, 2018), whereas the
630 upwelling Rossby waves take place during nIOD. During the nIOD events, the
631 positive wind stress curls anomalies force cyclonic current anomalies. As 2010 and
632 2016 are nIOD years and La Niña in 2010 is stronger than 2016, there are stronger
633 upwelling Rossby waves in 2011 than 2017, which make the thermocline shallow.
634 When the thermocline shoals, strengthened Ekman upwelling more easily brings the
635 high salinity and cold water into the upper layer, resulting in a decrease of local

636 precipitation. The processes are beneficial for the enhancement of the positive salinity
637 anomalies, so vertical entrainment caused by an anomalous cyclonic gyre maintains
638 high salinity anomalies during the decay phases of the nIOD and La Niña events.

639 Therefore, Ocean horizontal advection is the main factor of high salinity
640 anomaly variations during 10A11S and 16A17S. The entrainment effects in 2011 are
641 more significant than that in 2017 and the FWF has a negative and small effect on
642 positive salinity anomalies for two events. The mutual effects of horizontal advection,
643 FWF and vertical entrainment together lead to extremely high salinity anomalies in
644 the tropical central IO for two periods.

645 **4. Summary and Discussion**

646 Based on 2007-2018 Argo products and various satellite and reanalysis data,
647 there are significantly high salinity anomalies in the tropical central IO during
648 10A11S and 16A17S. The study provides a detailed description of spatial
649 characteristics of high salinity anomalies and the underlying formation mechanisms.
650 Salinity budget equation is performed to examine the role of surface buoyancy fluxes
651 and ocean dynamic processes.

652 Surface buoyancy fluxes and ocean dynamic processes are factors affecting the
653 high salinity anomalies for these two periods. The results show that the salinity
654 anomalies in 2010 autumn and 2017 spring are stronger than 2016 autumn and 2011
655 spring. But at the same time, the precipitation in the first two periods is also larger
656 than that in the latter two periods. The FWF changes and salinity anomaly variations
657 are inconsistent, so the impact of FWF has a small and negative contribution to the
658 high salinity anomalies for two periods. The analyses indicate that the high salinity
659 anomalies cannot be explained directly by the changes in regional air-sea freshwater
660 exchanges.

661 The co-occurrence of nIOD and La Niña in 2010 and 2016 is the main reason for
662 the occurrence of high salinity anomalies. The strong eastward currents caused by
663 nIOD and La Niña during September-December in 2010 and 2016 make high salinity
664 water transport eastward, triggering positively high salinity anomalies in the eastern

665 TIO. Additionally, during January-May in 2011 and 2017, which are the decay phases
666 of nIOD and La Niña, the westward currents transport the high salinity water of the
667 eastern IO westward, resulting in high salinity anomalies in the central IO. As La Niña
668 event is much stronger in 2010 than in 2016, the high salinity anomalies at the end of
669 2010 appear earlier and are stronger than 2016. Meanwhile, the decline of the former
670 lasts longer, so the salinity anomalies are gradually weakened in early 2011 while the
671 salinity anomalies decrease and then increase in early 2017. Therefore, the two-period
672 maximum salinity anomalies occur at different months, which are in January 2011 and
673 in March 2017, respectively. And the salinity anomalies from March to May in 2017
674 are more significant than that in 2011. On the other hand, when the nIOD and La Niña
675 events happen, the upwelling Rossby waves caused by cyclonic wind stress curls lead
676 to more cold and salty water entrained into the upper layer, causing the salinity to
677 increase. Due to the La Niña intensity in 2010 is stronger than in 2016, so the
678 entrainment effects in 2011 are stronger than that in 2017. These foregoing results can
679 be summarized by the sketch shown in Figure 14.

680 The results of the analyses in the study also verify the view that the interannual
681 variations of salinity in the TIO are mainly affected by IOD events. When a nIOD
682 event occurs, positive salinity anomalies caused by westerlies will occur at the end of
683 the year and the beginning of the next year. Depending on the intensities of the
684 occurrence of La Niña, positive salinity anomalies of different intensities will occur;
685 When a pIOD event occurs, the situation is the opposite and negative salinity
686 anomalies of different intensities will occur according to the intensities of the
687 occurrence of El Niño. Therefore, nIOD in 2010 and pIOD in 2011 result in positive
688 salinity anomalies during 10A11S and negative salinity anomalies from 2011 autumn
689 to 2012 spring, respectively. pIOD in 2015 and nIOD in 2016 result in negative
690 salinity anomalies during 15A16S and positive salinity anomalies during 16A17S,
691 respectively. Between the two periods of positive salinity anomalies (i.e. 2012-2016),
692 no strong pIOD events occur, so the salinity has been in negative anomalies or very
693 weak positive anomalies, that is, 2012-2016 is a period of freshening. However, why
694 there are no strong nIOD events during the periods? It may be related to the factors

695 such as the climate mode indexes or interdecadal oscillation. This is beyond the scope
696 of the study and left for further research.

697 In addition, through the quantitative analyses of the salinity budget equation, the
698 advection term is positive and maximum at the end of 2010, then becomes negative
699 and gradually weakens. During 16A17S, the advection term is relatively small, and
700 strong positive advection doesn't appear until the spring of 2017. The FWF has a
701 small and negative influence on salinity anomalies. Thus, we further conclude that
702 ocean advection is the main factor of positive salinity anomalies in the tropical central
703 IO. The positive salinity anomalies at the end of 2010 and 2016 are mainly due to the
704 positive zonal advection anomalies. The decrease in salinity anomalies in early 2011
705 is mainly caused by negative zonal current anomalies and the salinity anomalies in
706 early 2017 first decrease and then increase. They are similar to the results of the
707 previous ocean dynamic analyses. The upwelling generated by vertical entrainment
708 under the influence of nIOD and La Niña also has a certain impact on salinity and the
709 item has a greater impact in 2011 than in 2017. As a result, the mutual effects of
710 horizontal advection, FWF and vertical entrainment together lead to extremely high
711 salinity anomalies in the tropical central IO during 10A11S and 16A17S.

712 According to the salinity budget equation, in addition to the horizontal advection
713 term, the FWF term and the vertical entrainment term, there is one residual term ϵ . For
714 the residual term of the salinity budget, the main reason affecting the residual term is
715 that the data are from different sources. There is no dynamical balance among
716 different sources to keep a closed salinity budget. Various centers reconstruct the
717 observations from different sources using different methods, thus cause various errors.
718 The item generally includes some nonlinear terms such as horizontal and vertical
719 mixing disturbance, turbulent diffusion, and the accumulation of errors from the other
720 terms and so on, but these items are relatively complex. Here we only give the
721 qualitative analyses to understand the salinity anomalies. We need to obtain
722 higher-resolution data and improve the methods of computing all terms that contribute
723 to the salinity anomalies.

724 In short, due to the similar intensities of nIOD events in 2010 and 2016,

725 obviously positive salinity anomalies appear in the tropical central IO during 10A11S
726 and 16A17S. However, due to the significant difference in the intensities of the La
727 Niña events, the intensities of positive salinity anomalies for two periods are
728 significantly different. The co-occurrence of nIOD and strong La Niña in 2010 lead to
729 stronger positive zonal advection anomaly firstly and next negative zonal advection
730 anomaly, thus the negative contributions of zonal advection mainly lead to an
731 abnormal decrease in salinity during recession phases. The co-occurrence of nIOD
732 and weak La Niña in 2016 causes positive zonal advection anomaly firstly and next
733 negative zonal advection anomaly, and then positive zonal advection anomaly which
734 mainly result in extremely higher salinity anomalies in 2017 spring. The salinity
735 anomalies at the end of 2010 are stronger than that of 2016, and in 2017 spring are
736 stronger than that in 2011. Our results highlight the important role of the oceanic
737 dynamics in the salinity variability in the TIO. Given the known implications of
738 salinity anomalies on the upper-ocean stratification in the central-eastern TIO and
739 their potential impacts on air-sea interactions and climate variability there, the study
740 provides some new perspectives on the interannual variability of salinity in the TIO.

741 **Acknowledgements**

742 This study was supported by the Second Tibetan Plateau Scientific Expedition and
743 Research (STEP) program (Grant no. 2019QZKK0102), the Strategic Priority
744 Research Program of Chinese Academy of Sciences (Grant No. XDA20060500), the
745 Open Project Program of State Key Laboratory of Tropical Oceanography
746 (LTOZZ2102), the National Natural Science foundation of China (42176026) and the
747 Independent Research Project Program of State Key Laboratory of Tropical
748 Oceanography (LTOZZ2101).

749 **Data Availability Statement**

750 The gridded monthly Argo data were downloaded from
751 http://apdrc.soest.hawaii.edu/erddap/griddap/hawaii_soest_4daf_fed7_948a.html. The
752 ECMWF ORAS5 reanalysis data were retrieved from

753 http://apdrc.soest.hawaii.edu/erddap/griddap/hawaii_soest_3bf3_9d89_5708.html.
754 The SMAP salinity data were obtained from
755 http://apdrc.soest.hawaii.edu/erddap/griddap/hawaii_soest_0550_cd5c_d5bd.html.
756 The SODA salinity data were downloaded from
757 http://apdrc.soest.hawaii.edu/erddap/griddap/hawaii_soest_bb48_93c2_a711.html.
758 The SMOS salinity data were downloaded from <https://www.catds.fr/sipad/>. The
759 GPCP monthly precipitation data were available at
760 http://apdrc.soest.hawaii.edu/erddap/griddap/hawaii_soest_2d6e_67ad_91d2.html.
761 The OA Flux monthly evaporation data were available at
762 http://apdrc.soest.hawaii.edu/erddap/griddap/hawaii_soest_6b5a_df06_3eeb.html. The
763 ERSSTv5 SST analysis data were obtained from
764 http://apdrc.soest.hawaii.edu/erddap/griddap/hawaii_soest_31a3_72d5_401e.html.
765 The reanalysis data NCEP monthly pressure zonal wind and meridional wind were
766 extracted from
767 http://apdrc.soest.hawaii.edu/erddap/griddap/hawaii_soest_9bf0_875c_a184.html and
768 http://apdrc.soest.hawaii.edu/erddap/griddap/hawaii_soest_3c0a_cfec_e866.html,
769 respectively. The OFES model data were retrieved from
770 http://apdrc.soest.hawaii.edu/erddap/griddap/hawaii_soest_6c0d_24b8_6937.html for
771 zonal velocity and
772 http://apdrc.soest.hawaii.edu/erddap/griddap/hawaii_soest_c66b_2477_13c0.html for
773 meridional velocity. All data needed to evaluate the conclusions in the paper are
774 present in the paper and/or the Supplementary Materials. Additional data related to
775 this paper may be requested from the authors.

776 **References**

777 Adler, R. F., Huffman, G. J., Chang, A., Ferraro, R., Xie, P.-P., Janowiak, J., Rudolf, B.,
778 Schneider, U., Curtis, S., Bolvin, D., Gruber, A., Susskind, J., Arkin, P. and Nelkin, E.
779 (2003) The version-2 Global Precipitation Climatology Project (GPCP) monthly
780 precipitation analysis (1979-present). *Journal of Hydrometeorology*, 4, 1147-1167.
781 [https://doi.org/10.1175/1525-7541\(2003\)004%3C1147:TVGPCP%3E2.0.CO;2](https://doi.org/10.1175/1525-7541(2003)004%3C1147:TVGPCP%3E2.0.CO;2).
782 Bhavani, T. S. D., Chowdary, J. S., Bharathi, G., Srinivas, G., Prasad, K. V. S. R., Deshpande,

783 A., Parekh, A. and Gnanaseelan, C. (2017) Response of the tropical Indian Ocean SST to
784 decay phase of La Niña and associated processes. *Dynamics of Atmospheres and Oceans*,
785 80, 110-123. <https://doi.org/10.1016/j.dynatmoce.2017.10.005>.

786 Burns, J. M. and Subrahmanyam, B. (2016) Variability of the Seychelles-Chagos Thermocline
787 Ridge dynamics in connection with ENSO and Indian Ocean Dipole. *IEEE Geoscience
788 and Remote Sensing Letters*, 13, 2019-2023.
789 <https://doi.org/10.1109/LGRS.2016.2621353>.

790 Cai, W., Pan, A., Roemmich, D., Cowan, T. and Guo, X. (2009) Argo profiles a rare
791 occurrence of three consecutive positive Indian Ocean Dipole events, 2006-2008.
792 *Geophysical Research Letters*, 36, L08701. <https://doi.org/10.1029/2008GL037038>.

793 Clarke, A. J. and Liu, X. (1994) Interannual sea level in the northern and eastern Indian Ocean.
794 *Journal of Physical Oceanography*, 24, 1224-1235.
795 [https://doi.org/10.1175/1520-0485\(1994\)024<1224:ISLITN>2.0.CO;2](https://doi.org/10.1175/1520-0485(1994)024<1224:ISLITN>2.0.CO;2).

796 Delcroix, T. and Hénin, C. (1991) Seasonal and interannual variations of sea surface salinity
797 in the tropical Pacific Ocean. *Journal of Geophysical Research*, 96, 22, 135-22, 150.
798 <https://doi.org/10.1029/91JC02124>.

799 Durack, P. J. and Wijffels, S. E. (2010) Fifty-year trends in global ocean salinities and their
800 relationship to broad-scale warming. *Journal of Climate*, 23, 4342-4362.
801 <https://doi.org/10.1175/2010JCLI3377.1>.

802 Durack, P. J., Wijffels, S. E. and Matear, R. J. (2012) Ocean salinities reveal strong global
803 water cycle intensification during 1950-2000. *Science*, 336, 455-458.
804 <https://doi.org/10.1126/science.1212222>.

805 Du, Y. and Zhang, Y. H. (2015) Satellite and Argo observed surface salinity variations in the
806 tropical Indian Ocean and their association with the Indian Ocean Dipole Mode. *Journal
807 of Climate*, 28, 695-713. <https://doi.org/10.1175/JCLI-D-14-00435.1>.

808 Du, Y., Xie, S.-P., Huang, G. and Hu, K. (2009) Role of air-sea interaction in the long
809 persistence of El Niño-induced North Indian Ocean warming. *Journal of Climate*, 22,
810 2023-2038. <https://doi.org/10.1175/2008jcli2590.1>.

811 Feng, M., Meyers, G., Pearce, A. and Wijffels, S. (2003) Annual and interannual variations of
812 the Leeuwin Current at 32°S. *Journal of Geophysical Research*, 108, 3355.
813 <https://doi.org/10.1029/2002JC001763>.

814 Feng, M., McPhaden, M. J. and Lee, T. (2010) Decadal variability of the Pacific subtropical
815 cells and their influence on the southeast Indian Ocean. *Geophysical Research Letters*,
816 37, L09606. <https://doi.org/10.1029/2010GL042796>.

817 Font, J., Camps, A., Borges, A., Martín-Neira, M., Boutin, J., Reul, N., H. Kerr, Y., Hahne, A.
818 and Mecklenburg, S. (2010) SMOS: the challenging sea surface salinity measurement
819 from space. *Proceedings of the IEEE*, 98, 649-665.
820 <https://doi.org/10.1109/JPROC.2009.2033096>.

821 Fore, A., Yueh, S., Tanh, W. and Hayashi, A. (2020) JPL SMAP Ocean Surface Salinity

822 Products [Level 2B, Level 3 Running 8-day, Level 3 Monthly], Version 5.0 validated
823 release. *Jet Propulsion Laboratory*, Pasadena, CA, USA.

824 Gao, S., Qu, T. and Nie, X. (2014) Mixed layer salinity budget in the tropical Pacific Ocean
825 estimated by a global GCM. *Journal of Geophysical Research: Oceans*, 119, 8255-8270.
826 <https://doi.org/10.1002/2014JC010336>.

827 Gnanaseelan, C., Deshpande, A. and McPhaden, M. J. (2012) Impact of Indian Ocean Dipole
828 and El Niño/Southern Oscillation wind-forcing on the Wyrтки jets. *Journal of*
829 *Geophysical Research*, 117, C08005. <https://doi.org/10.1029/2012JC007918>.

830 Gould, J., Roemmich, D., Wijffels, S., Freeland, H., Ignaszewsky, M., Xu, J., Pouliquen, S.,
831 Desaubies, Y., Send, U., Radjalrishnan, K., Takeuchi, K., Kim, K., Danchenkov, M.,
832 Sutton, P., King, B., Owens, B. and Riser, S. (2004) Argo profiling floats bring new era
833 of in situ ocean observations. *Eos, Transactions of the American Geophysical Union*, 85,
834 185-191. <https://doi.org/10.1029/2004EO190002>.

835 Grunseich, G., Subrahmanyam, B. and Wang, B. (2013) The Madden-Julian oscillation
836 detected in Aquarius salinity observations. *Geophysical Research Letters*, 40, 5461-5466.
837 <https://doi.org/10.1002/2013GL058173>.

838 Grunseich, G., Subrahmanyam, B., Murty, V. S. N. and Giese, B. S. (2011) Sea surface
839 salinity variability during the Indian Ocean Dipole and ENSO events in the tropical
840 Indian Ocean. *Journal of Geophysical Research*, 116, C11013.
841 <https://doi.org/10.1029/2011JC007456>.

842 Guan, B., Lee, T., Halkides, D. J. and Waliser, D. E. (2014) Aquarius surface salinity and the
843 Madden-Julian Oscillation: The role of salinity in surface layer density and potential
844 energy. *Geophysical Research Letters*, 41, 2858-2869.
845 <https://doi.org/10.1002/2014GL059704>.

846 Hasson, A., Delcroix, T., Boutin, J., Dussin, R. and Ballabrera-Poy, J. (2014) Analyzing the
847 2010-2011 La Niña signature in the tropical Pacific sea surface salinity using in situ data,
848 SMOS observations, and a numerical simulation. *Journal of Geophysical Research:*
849 *Oceans*, 119, 3855-3867. <https://doi.org/10.1002/2013JC009388>.

850 Hasson, A. E. A., Delcroix, T. and Dussin, R. (2013) An assessment of the mixed layer
851 salinity budget in the tropical Pacific Ocean. Observations and modelling (1990-2009).
852 *Ocean Dynamics*, 63, 179-194. <https://doi.org/10.1007/s10236-013-0596-2>.

853 Hong, C.-C., Lu, M.-M. and Kanamitsu, M. (2008) Temporal and spatial characteristics of
854 positive and negative Indian Ocean dipole with and without ENSO, *Journal of*
855 *Geophysical Research*, 113, D08107. <https://doi.org/10.1029/2007JD009151>.

856 Horii, T., Ueki, I., Ando, K., Hasegawa, T., Mizuno, K. and Seiki, A. (2016) Impact of
857 intraseasonal salinity variations on sea surface temperature in the eastern equatorial
858 Indian Ocean. *Journal of Oceanography*, 72, 313-326.
859 <https://doi.org/10.1007/s10872-015-0337-x>.

860 Huffman, G. J., Adler, R. F., Bolvin, D. T. and Gu, G. (2009) Improving the global

861 precipitation record: GPCP version 2.1. *Geophysical Research Letters*, 36, L17808.
862 <https://doi.org/10.1029/2009GL040000>.

863 Jensen, T. G. (2003) Cross-equatorial pathways of salt and tracers from the northern Indian
864 Ocean: Modelling results. *Deep-Sea Research Part II*, 50, 2111-2127.
865 [https://doi.org/10.1016/S0967-0645\(03\)00048-1](https://doi.org/10.1016/S0967-0645(03)00048-1).

866 Kido, S. and Tozuka, T. (2017) Salinity Variability Associated with the Positive Indian Ocean
867 Dipole and Its Impact on the Upper Ocean Temperature. *Journal of Climate*, 30,
868 7885-7907. <https://doi.org/10.1175/JCLI-D-17-0133.1>.

869 Kido, S., Tozuka, T. and Han, W. (2019) Anatomy of salinity anomalies associated with the
870 positive Indian Ocean Dipole. *Journal of Geophysical Research: Oceans*, 124,
871 8116-8139. <https://doi.org/10.1029/2019JC015163>.

872 Lagerloef, G. S. E. (2002) Introduction to the special section: The role of surface salinity on
873 upper ocean dynamics, air-sea interaction and climate. *Journal of Geophysical Research*,
874 107, 8000. <https://doi.org/10.1029/2002JC001669>.

875 Li, J., Liang, C., Tang, Y., Liu, X., Lian, T., Shen, Z. and Li, X. (2018) Impacts of the
876 IOD-associated temperature and salinity anomalies on the intermittent equatorial
877 undercurrent anomalies. *Climate Dynamics*, 51, 1391-1409.
878 <https://doi.org/10.1007/s00382-017-3961-x>.

879 Liang, Z., Xie, Q., Zeng, L. and Wang, D. (2018) Role of wind forcing and eddy activity in
880 the intraseasonal variability of the barrier layer in the South China Sea. *Ocean Dynamics*,
881 68, 363-375. <https://doi.org/10.1007/s10236-018-1137-9>.

882 Martins, M. S. and Stammer, D. (2015) Pacific Ocean surface freshwater variability
883 underneath the double ITCZ as seen by satellite sea surface salinity retrievals. *Journal of*
884 *Geophysical Research: Oceans*, 120, 5870-5885. <https://doi.org/10.1002/2015JC010895>.

885 Masumoto, Y., Sasaki, H., Kagimoto, T., Komori, N., Ishida, A., Sasai, Y., Miyama, Y., Motoi,
886 T., Mitsudera, N., Takahashi, K., Sakuma, H. and Yamagata, T. (2004) A fifty-year
887 eddy-resolving simulation of the world ocean—Preliminary outcomes of OFES (OGCM
888 for the Earth Simulator). *Journal of the Earth Simulator*, 1, 35-56.
889 <https://www.researchgate.net/publication/242679951>.

890 Mecklenburg, S., Kerr, Y., Font, J. and Hahne, A. (2008) The Soil Moisture and Ocean
891 Salinity (SMOS) mission—an overview. *IEEE International Geoscience and Sensing*
892 *Symposium*, 10, IV-938-IV-941. <https://doi.org/10.1109/IGARSS.2008.4779878>.

893 Meyers, G. (1996) Variation of Indonesian throughflow and the El Niño-Southern Oscillation.
894 *Journal of Geophysical Research*, 101, 12, 255-12, 263.
895 <https://doi.org/10.1029/95JC03729>.

896 Murtugudde, R., McCreary, J. P. and Busalacchi, A. J. (2000) Oceanic processes associated
897 with anomalous events in the Indian Ocean with relevance to 1997-1998. *Journal of*
898 *Geophysical Research*, 105, 3295-3306. <https://doi.org/10.1029/1999JC900294>.

899 Nyadjro, E. S. and Subrahmanyam, B. (2014) SMOS salinity mission reveals salinity

900 structure of the Indian Ocean Dipole. *IEEE Geoscience and Remote Sensing Letters*, 11,
901 1564-1568, <https://doi.org/10.1109/LGRS.2014.2301594>.

902 Nyadjro, E. S., Subrahmanyam, B., Murty, V. S. N. and Shriver, J. F. (2012) The role of
903 salinity on the dynamics of the Arabian Sea mini warm pool. *Journal of Geophysical*
904 *Research*, 117, C09002. <https://doi.org/10.1029/2012JC007978>.

905 Phillips, H. E., Tandon, A., Furue, R., Hood, R., Ummenhofer, C. C., Benthuisen, J. A.,
906 Menezes, V., Hu, S., Webber, B., Sanchez-Franks, A., Cherian, D., Shroyer, E., Feng, M.,
907 Wijesekera, H., Chatterjee, A., Yu, L., Hermes, J., Murtugudde, R., Tozuka, T., Su, D.,
908 Singh, A., Centurioni, L., Prakash, S. and Wiggert, J. (2021) Progress in understanding
909 of Indian Ocean circulation, variability, air-sea exchange, and impacts on
910 biogeochemistry. *Ocean Science*, 17, 1677-1751.
911 <https://doi.org/10.5194/os-17-1677-2021>.

912 Qu, T., Gao, S. and Fukumori, I. (2013) Formation of salinity maximum water and its
913 contribution to the overturning circulation in the North Atlantic as revealed by a global
914 general circulation model. *Journal of Geophysical Research: Oceans*, 118, 1982-1994.
915 <https://doi.org/10.1002/jgrc.20152>.

916 Rao, R. R. and Sivakumar, R. (2003) Seasonal variability of sea surface salinity and salt
917 budget of the mixed layer of the north Indian Ocean. *Journal of Geophysical Research*,
918 108, 3009. <https://doi.org/10.1029/2001JC000907>.

919 Ren, L. and Riser, S. C. (2009) Seasonal salt budget in the northeast Pacific Ocean. *Journal of*
920 *Geophysical Research*, 114, C12004. <https://doi.org/10.1029/2009JC005307>.

921 Ren, L., Speer, K. and Chassignet, E. P. (2011) The mixed layer salinity budget and sea ice in
922 the Southern Ocean. *Journal of Geophysical Research*, 116, C08031.
923 <https://doi.org/10.1029/2010JC006634>.

924 Reppin, J., Schott, F. A., Fischer, J. and Quadfasel, D. (1999) Equatorial currents and
925 transports in the upper central Indian Ocean: Annual cycle and interannual variability.
926 *Journal of Geophysical Research*, 104, 15495-15514.
927 <https://doi.org/10.1029/1999JC900093>.

928 Riser, S. C., Ren, L. and Wong, A. (2008) Salinity in Argo: A modern view of a changing
929 ocean. *Oceanography*, 21, 56-67. <https://doi.org/10.5670/oceanog.2008.67>.

930 Roemmich, D. and the Argo Steering Team. (2009) Argo: The challenge of continuing 10
931 years of progress. *Oceanography*, 22, 46-55. <https://doi.org/10.5670/oceanog.2009.65>.

932 Roemmich, D. and Owens, W. B. (2000) The Argo project: Global ocean observations for
933 understanding and prediction of climate variability. *Oceanography*, 13, 45-50.
934 <https://doi.org/10.5670/oceanog.2000.33>.

935 Saji, N. H., Goswami, B. N., Vinayachandran, P. N. and Yamagata, T. (1999) A dipole mode in
936 the tropical Indian Ocean. *Nature*, 401, 360-363. <https://www.nature.com/articles/43854>.

937 Saji, N. H. and Yamagata, T. (2003) Possible impacts of Indian Ocean Dipole mode events on
938 global climate. *CLIMATE RESEARCH*, 25, 151-169.

939 <https://www.jstor.org/stable/24868393>.

940 Sasaki, Y., Ishida, A., Yamanaka, Y. and Sasaki, H. (2004) Chlorofluorocarbons in a global
941 ocean eddy-resolving OGCM: Pathway and formation of Antarctic Bottom Water.
942 *Geophysical Research Letters*, 31, L12305. <https://doi.org/10.1029/2004GL019895>.

943 Schiller, A., Mikolajewicz, U. and Voss, R. (1997) The stability of the North Atlantic
944 thermohaline circulation in a coupled ocean-atmosphere general circulation model.
945 *Climate Dynamics*, 13, 325-347. <https://doi.org/10.1007/s003820050169>.

946 Schmitt, R. N. W. (2008) Salinity and the global water cycle. *Oceanography*, 21, 12-19.
947 <https://doi.org/10.5670/oceanog.2008.63>.

948 Schmitt, R. W. and Blair, A. (2015) A river of salt. *Oceanography*, 28, 40-45.
949 <https://doi.org/10.5670/oceanog.2015.04>.

950 Schott, F. A., Xie, S.-P. and McCreary, J. P. (2009) Indian Ocean circulation and climate
951 variability. *Reviews of Geophysical*, 47, RG1002.
952 <https://doi.org/10.1029/2007RG000245>.

953 Sharma, R., Agarwal, N., Momin, I. M., Basu, S. and Agarwal, V. K. (2010) Simulated Sea
954 Surface Salinity Variability in the Tropical Indian Ocean. *Journal of Climate*, 23,
955 6542-6554. <https://doi.org/10.1175/2010JCLI3721.1>.

956 Sharma, S., Kumari, A., Navajyoth, M. P., Kumar, P. and Saharwardi, M. S. (2020) Impact of
957 air-sea interaction during two contrasting monsoon seasons. *Theoretical and Applied*
958 *Climatology*, 141, 1645-1659. <https://doi.org/10.1007/s00704-020-03300-6>.

959 Simon, B., Rahman, S. H. and Joshi, P. C. (2006) Conditions leading to the onset of the Indian
960 monsoon: A satellite perspective. *Meteorology and Atmospheric Physics*, 93, 201-210.
961 <https://doi.org/10.1007/s00703-005-0155-6>.

962 Skliris, N., Marsh, R., Josey, S. A., Good, S. A., Liu, C. and Allan, R. P. (2014) Salinity
963 changes in the World Ocean since 1950 in relation to changing surface freshwater fluxes.
964 *Climate Dynamics*, 43, 709-736. <https://doi.org/10.1007/s00382-014-2131-7>.

965 Stammer, D. (1997) Global characteristics of ocean variability estimated from regional
966 TOPEX/POSEIDON altimeter measurements. *Journal of physical oceanography*, 27,
967 1743-1769. [https://doi.org/10.1175/1520-0485\(1997\)027<1743:GCOOVE>2.0.CO;2](https://doi.org/10.1175/1520-0485(1997)027<1743:GCOOVE>2.0.CO;2).

968 Stuecker, M. F., Timmermann, A., Jin, F.-F., Chikamoto, Y., Zhang, W., Wittenberg, A. T.,
969 Widiasih, E. and Zhao, S. (2017) Revisiting ENSO/Indian Ocean Dipole phase
970 relationships. *Geophysical Research Letters*, 44, 2481-2492.
971 <https://doi.org/10.1002/2016GL072308>.

972 Subrahmanyam, B., Murty, V. S. N. and Heffner, D. M. (2011) Sea Surface Salinity Variability
973 in the Tropical Indian Ocean. *Remote Sensing of Environment*, 115, 944-956.
974 <https://doi.org/10.1016/j.rse.2010.12.004>.

975 Sun, Q., Du, Y., Zhang, Y., Feng, M., Chowdary, J. S., Chi, J., Qiu, S. and Yu, W. (2019)
976 Evolution of sea surface salinity anomalies in the southwestern tropical Indian Ocean
977 during 2010-2011 influenced by a negative IOD event. *Journal of Geophysical Research:*

978 *Oceans*, 124, 3428-3445. <https://doi.org/10.1029/2018JC014580>.

979 Sun, S., Lan, J., Fang, Y., Tana and Gao, X. (2015) A triggering mechanism for the Indian
980 Ocean Dipoles independent of ENSO. *Journal of Climate*, 28, 5063-5076.
981 <https://journals.ametsoc.org/view/journals/clim/28/13/jcli-d-14-00580.1.xml>.

982 Thompson, B., Gnanaseelan, C. and Salvekar, P. S. (2006) Variability in the Indian Ocean
983 circulation and salinity and its impact on SST anomalies during dipole events. *Journal of*
984 *Marine Research*, 64, 853-880. <https://doi.org/10.1357/002224006779698350>.

985 Tozuka, T., Yokoi, T. and Yamagata, T. (2010) A modeling study of interannual variations of
986 the seychelles dome. *Journal of Geophysical Research*, 115, C04005.
987 <https://doi.org/10.1029/2009JC005547>.

988 Vinayachandran, P. N. and Nanjundiah, R. S. (2009) Indian Ocean sea surface salinity
989 variations in a coupled model. *Climate Dynamics*, 33, 245-263.
990 <https://doi.org/10.1007/s00382-008-0511-6>.

991 Wang, B., Wu, R. and Li, T. (2003) Atmosphere-warm ocean interaction and its impacts on
992 Asian-Australian monsoon variation. *Journal of Climate*, 16, 1195-1211.
993 [https://doi.org/10.1175/1520-0442\(2003\)16%3C1195:AOIAII%3E2.0.CO;2](https://doi.org/10.1175/1520-0442(2003)16%3C1195:AOIAII%3E2.0.CO;2).

994 Wijffels, S. and Meyers, G. (2004) An intersection of oceanic waveguides: Variability in the
995 Indonesian Throughflow region. *Journal of Physical Oceanography*, 34, 1232-1253.
996 [https://doi.org/10.1175/1520-0485\(2004\)034%3C1232:AIOOWV%3E2.0.CO;2](https://doi.org/10.1175/1520-0485(2004)034%3C1232:AIOOWV%3E2.0.CO;2).

997 Williams, P. D., Guilyardi, E., Madec, G., Gualdi, S. and Scoccimarro, E. (2010) The role of
998 mean ocean salinity in climate. *Dynamics of Atmospheres and Oceans*, 49, 108-123.
999 <https://doi.org/10.1016/j.dynatmoce.2009.02.001>.

1000 Wyrski, K. (1973) An equatorial jet in the Indian Ocean. *Science*, 181, 262-264.
1001 <https://doi.org/10.1126/science.181.4096.262>.

1002 Xie, S.-P., Annamalai, H., Schott, F. A. and McCreary, J. P. (2002) Structure and mechanism
1003 of South Indian Ocean climate variability. *Journal of Climate*, 15, 864-878.
1004 [https://doi.org/10.1175/1520-0442\(2002\)0152.0.CO;2](https://doi.org/10.1175/1520-0442(2002)0152.0.CO;2).

1005 Xie, S.-P., Hu, K., Hafner, J., Tokinaga, H., Du, Y., Huang, G. and Sampe, T. (2009) Indian
1006 Ocean capacitor effect on Indo-western Pacific climate during the summer following El
1007 Niño. *Journal of Climate*, 22, 730-747. <https://doi.org/10.1175/2008JCLI2544.1>.

1008 Yadav, R. K. and Roxy, M. K. (2019) On the relationship between north India summer
1009 monsoon rainfall and east equatorial Indian Ocean warming. *Global and Planetary*
1010 *Change*, 179, 23-32. <https://doi.org/10.1016/j.gloplacha.2019.05.001>.

1011 Yokoi, T., Tozuka, T. and Yamagata, T. (2008) Seasonal variation of the Seychelles Dome.
1012 *Journal of Climate*, 21, 3740-3754. <https://doi.org/10.1175/2008JCLI1957.1>.

1013 Yokoi, T., Tozuka, T. and Yamagata, T. (2012) Seasonal and interannual variations of the SST
1014 above the Seychelles Dome. *Journal of Climate*, 25, 800-814.
1015 <https://doi.org/10.1175/JCLI-D-10-05001.1>.

1016 Yu, L. and Rienecker, M. M. (1999) Mechanisms for the Indian Ocean warming during the

1017 1997-98 El Niño. *Geophysical Research Letters*, 26, 735-738.
1018 <https://doi.org/10.1029/1999GL900072>.

1019 Yu, L. and Weller, R. A. (2007) Objectively analyzed air-sea heat fluxes for the global ice-free
1020 oceans (1981-2005). *American Meteorological Society*, 88, 527-540.
1021 <https://doi.org/10.1175/BAMS-88-4-527>.

1022 Yu, W., Xiang, B., Liu, L. and Liu, N. (2005) Understanding the origins of interannual
1023 thermocline variations in the tropical Indian Ocean. *Geophysical Research Letters*, 32,
1024 L24706. <https://doi.org/10.1029/2005GL024327>.

1025 Zeng, L. and Wang, D. (2017) Seasonal variations in the barrier layer in the South China Sea:
1026 characteristics, mechanisms and impact of warming. *Climate Dynamics*, 48, 1911-1930.
1027 <https://doi.org/10.1007/s00382-016-3182-8>.

1028 Zhang, L., Du, Y. and Cai, W. (2018) Low-frequency variability and the unusual Indian Ocean
1029 Dipole events in 2015 and 2016. *Geophysical Research Letters*, 45, 1040-1048.
1030 <https://doi.org/10.1002/2017GL076003>.

1031 Zhang, Y., Du, Y., Jayarathna, W. N. D. S., Sun, Q., Zhang, Y., Yao, F. and Feng, M. (2020) A
1032 prolonged high-salinity event in the Northern Arabian Sea during 2014-2017. *Journal of*
1033 *Physical Oceanography*, 50, 849-865. <https://doi.org/10.1175/JPO-D-19-0220.1>.

1034 Zhang, Y., Du, Y., Zheng, S., Yang, Y. and Cheng, X. (2013) Impact of Indian Ocean dipole on
1035 the salinity budget in the equatorial Indian Ocean. *Journal of Geophysical Research:*
1036 *Oceans*, 118, 4911-4923. <https://doi.org/10.1002/jgrc.20392>.

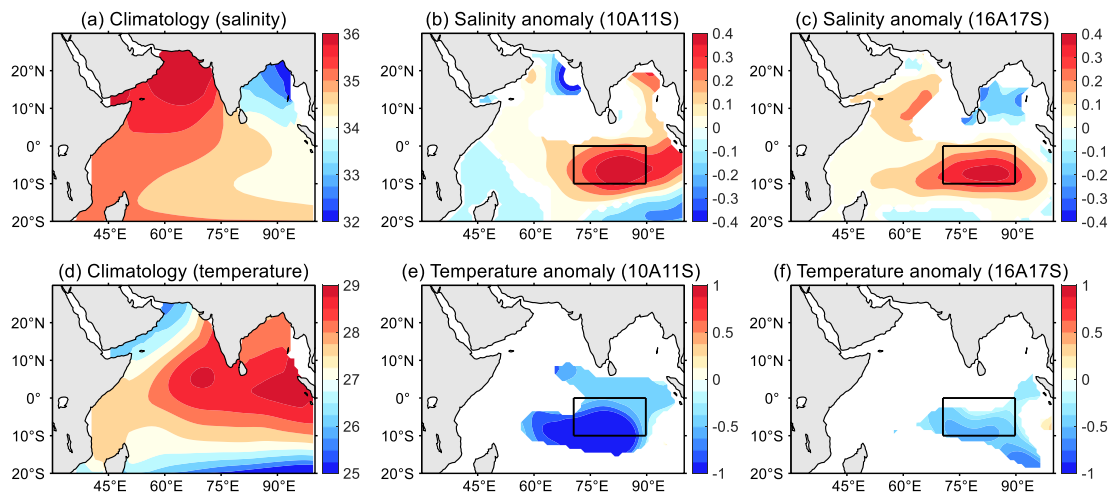


Figure 1. Annual climatological mean spatial distribution of the upper (a) salinity (unit: psu) and (d) temperature (unit: °C) in the tropical and subtropical IO based on the Argo data from 2007-2018; The spatial distributions of salinity anomaly (unit: psu) in the above areas during (b) 10A11S and (c) 16A17S. (e) and (f) are the same as (b) and (c), but for temperature anomaly (unit: °C). Only the anomalies exceeding the 95% confidence level based on a Student's t-test are shown. The black closed boxes in (b) and (c) denote the main area with positive salinity anomalies and in (e) and (f) indicate the position corresponding to the positive salinity anomalies.

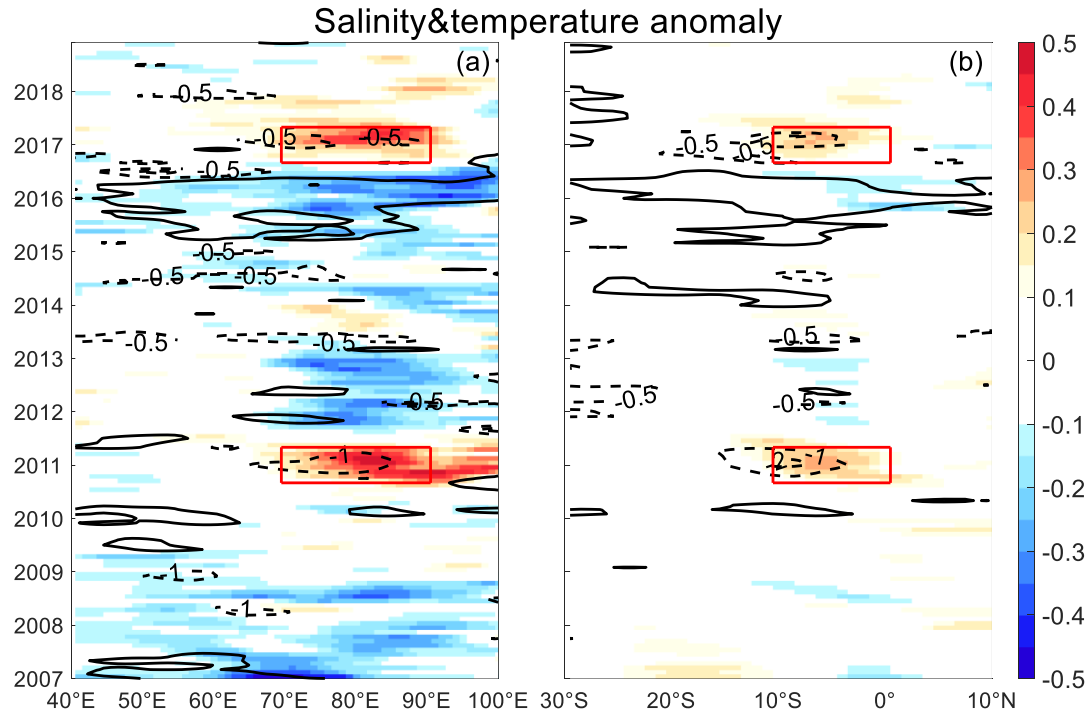


Figure 2. Hovmöller diagrams of salinity anomaly (shading, unit: psu) and temperature anomaly (contours, unit: °C) along (a) zonal section, averaged meridionally in 10°S-0° and (b) meridional section, averaged zonally in 70°E-90°E based on the Argo data during 2007-2018. The red boxes represent the extremely high salinity anomalies during 10A11S and 16A17S.

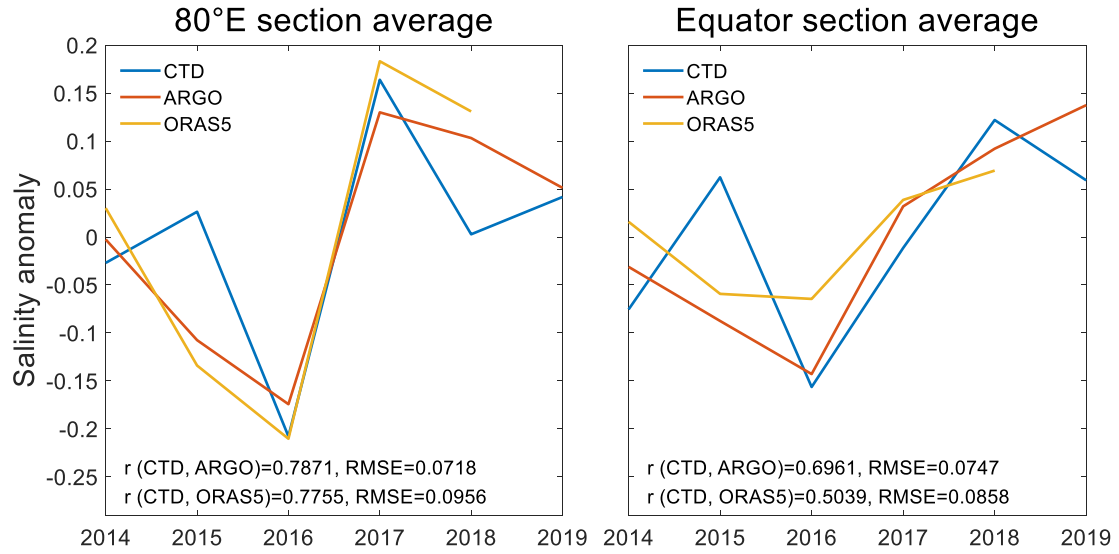


Figure 3. Comparisons between the time series of the CTD (blue), ARGO (red), ECMWF ORAS5 (yellow) salinity anomaly (unit: psu) area-averaged at 80°E (left) and equator (right) sections from 2014 to 2019. The correlation coefficients and RMSEs between the time series are estimated for the periods both the data are available.

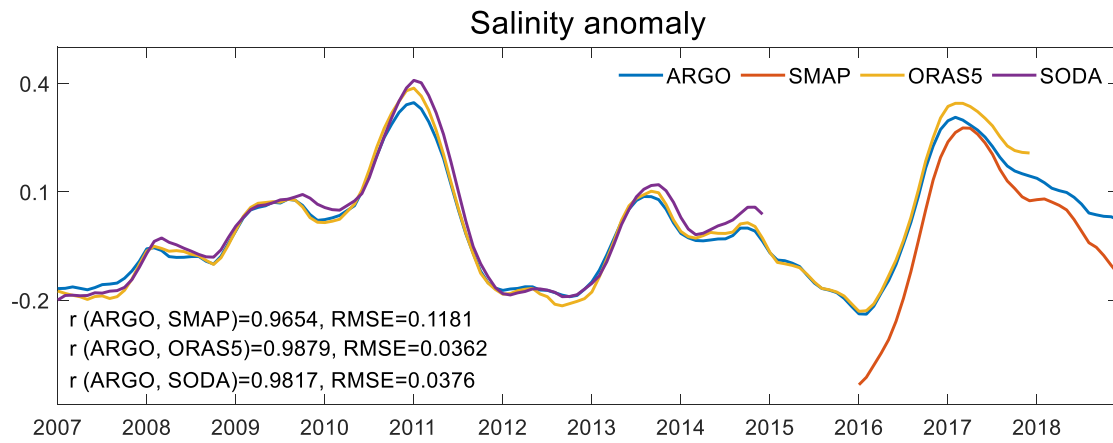


Figure 4. Comparisons between the time series of the ARGO (blue), SMAP (red), ECMWF ORAS5 (yellow) and SODA (purple) salinity anomaly (unit: psu) area-averaged from 2007 to 2018. The correlation coefficients and RMSEs between the time series are estimated for the periods both the data are available.

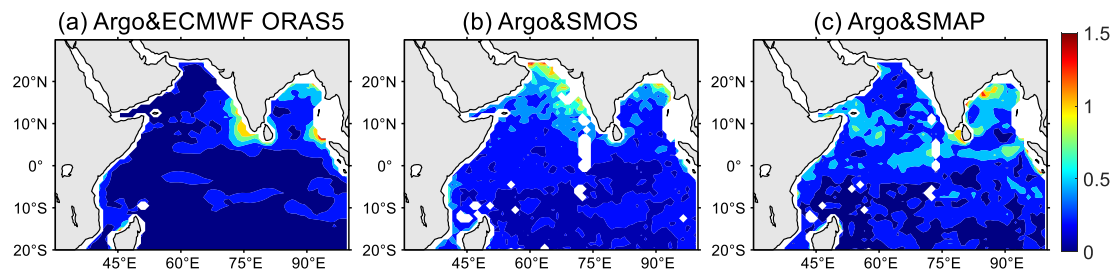


Figure 5. The spatial distributions of salinity RMSEs (a) between Argo and ECMWF ORAS5 data, (b) between Argo and SMOS data, (c) between Argo and SMAP data.

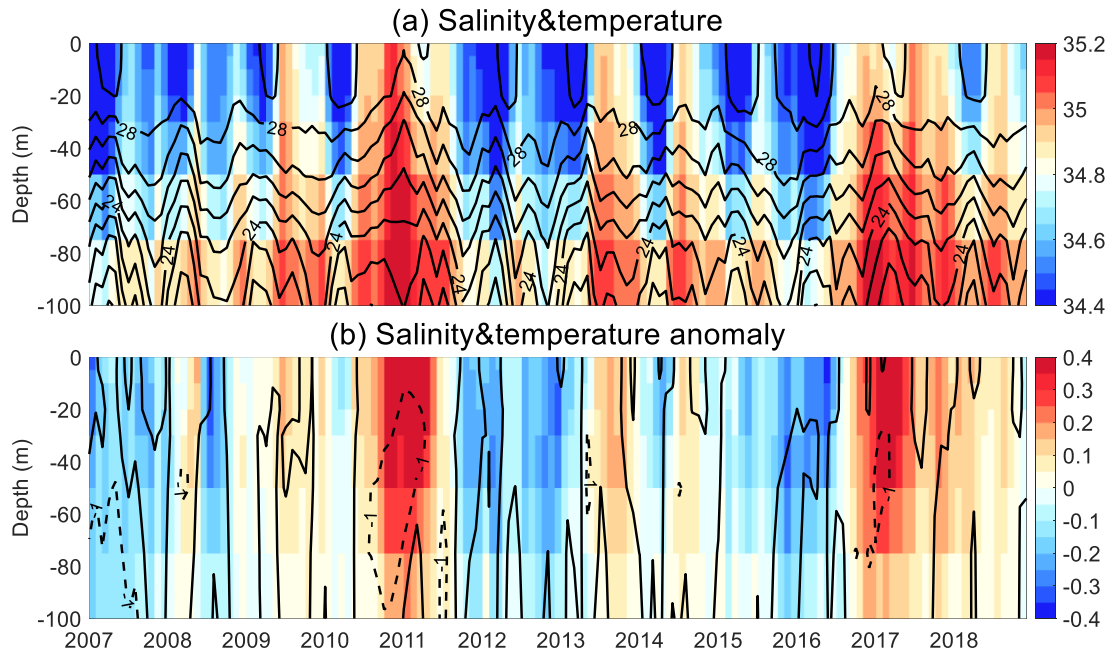


Figure 6. Time-depth distributions of area-averaged (a) salinity (shading) and temperature (contours) and (b) salinity anomaly (shading, unit: psu) and temperature anomaly (contours, unit: °C) from 2007 to 2018 based on the Argo data.

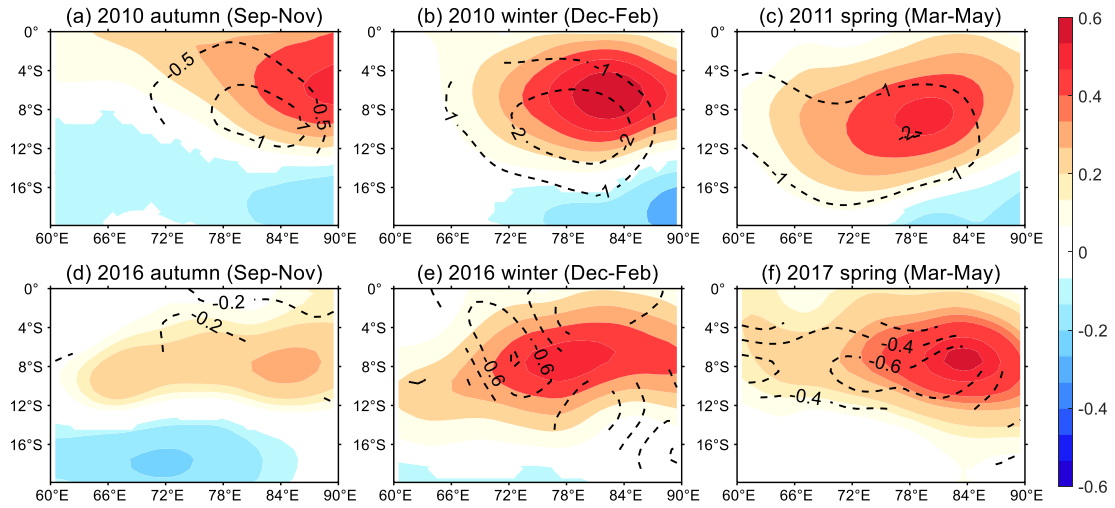


Figure 7. Spatial distributions of three-month moving mean high salinity anomaly (shading, unit: psu) and SSTA (contours, unit: °C) during (a-c) 10A11S and (d-f) 16A17S based on the Argo data in the main high salinity anomaly area. Only the anomalies exceeding the 95% confidence level based on a Student's t-test are shown.

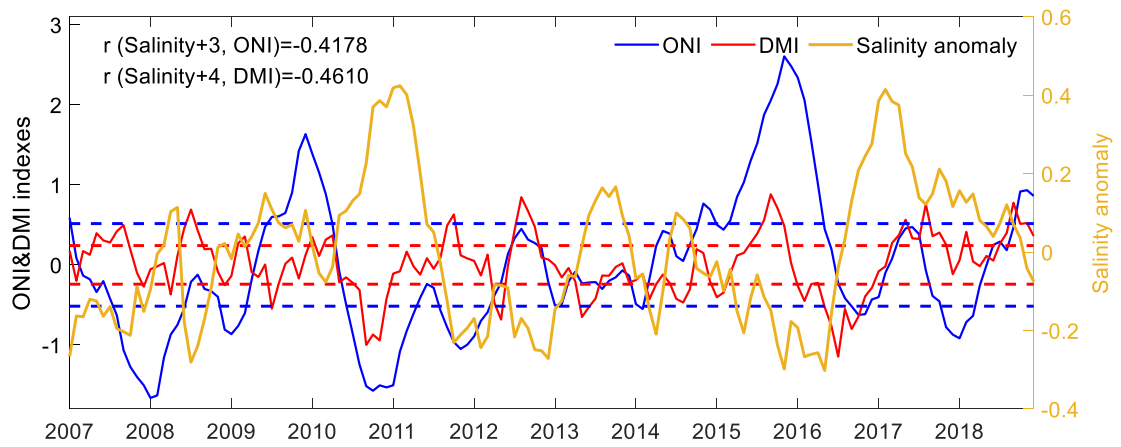


Figure 8. Time series of the ONI (blue curve) and DMI (red curve) indexes (unit: °C) in 2007-2018. The blue and red dashed lines denote the threshold of ± 0.5 times the standard deviation for ONI and DMI, respectively. The yellow curve denotes the time series of salinity anomaly (unit: psu) area-averaged in 70°E-90°E, 10°S-0°.

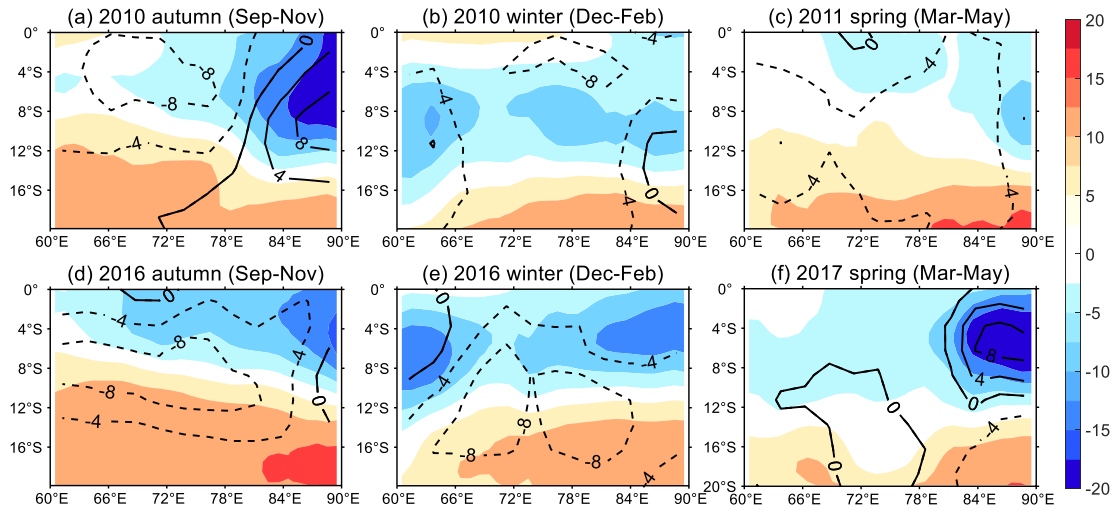


Figure 9. Spatial distributions of cumulative precipitation anomaly (contours, unit: mm per day) and surface FWF (i.e. evaporation minus precipitation; shading, unit: mm per day) in three months during (a-c) 10A11S and (d-f) 16A17S.

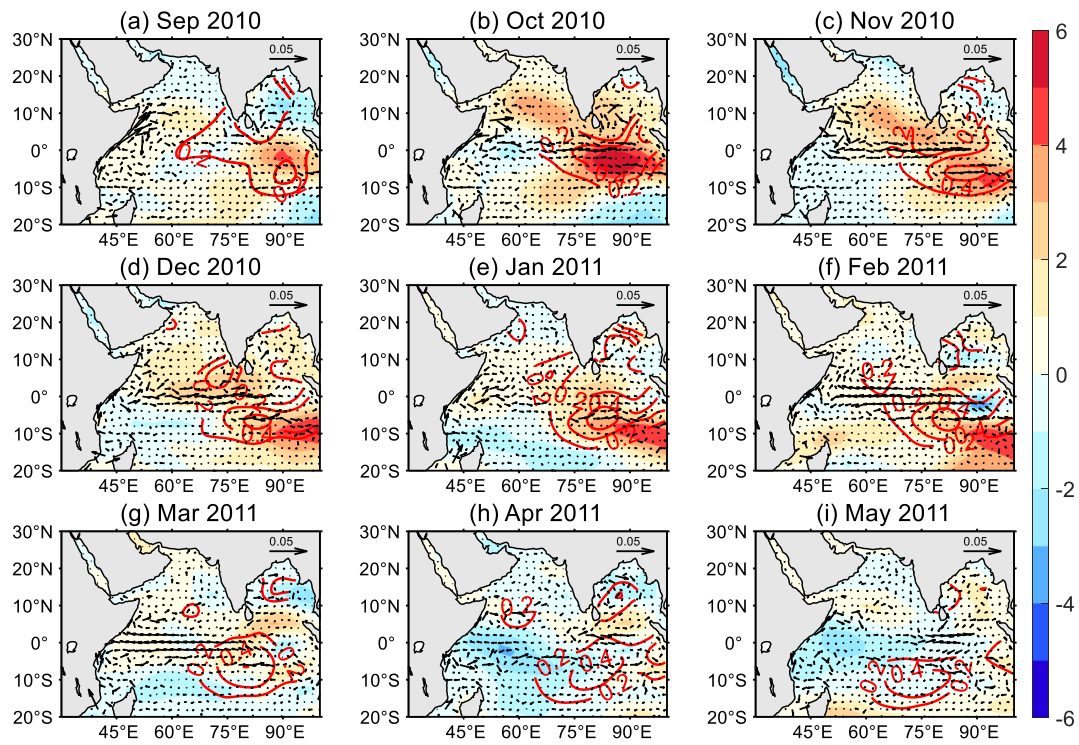


Figure 10. Spatial distributions of monthly mean Argo salinity anomaly (red contours, unit: psu), ocean current (vectors, unit: m s^{-1}) and zonal wind anomaly (shading, unit: m s^{-1}) during 10A11S. Positive zonal wind anomalies indicate westerlies.

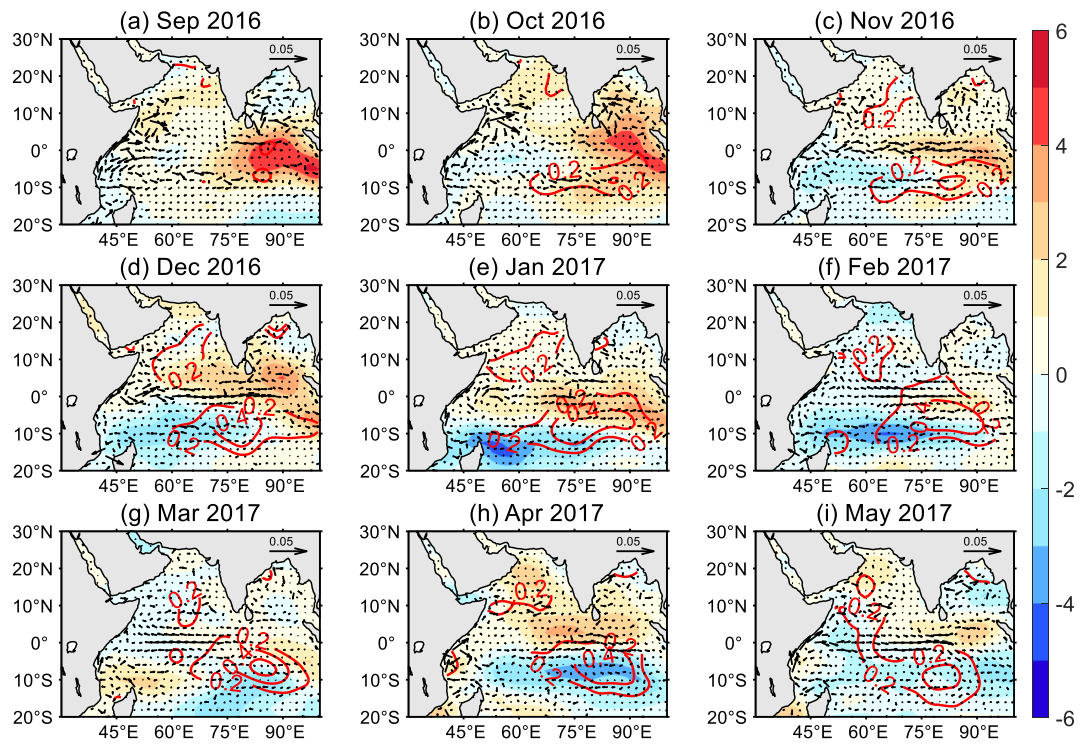


Figure 11. Same as Figure 10, but during 16A17S.

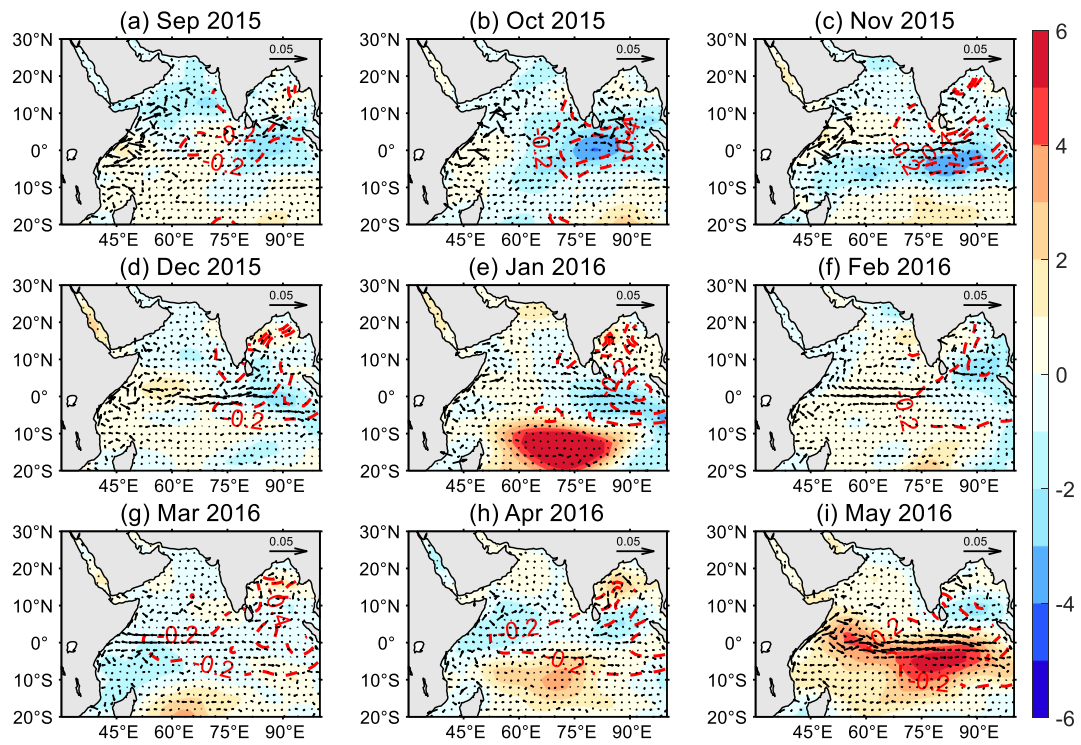


Figure 12. Same as Figure 10, but during 15A16S.

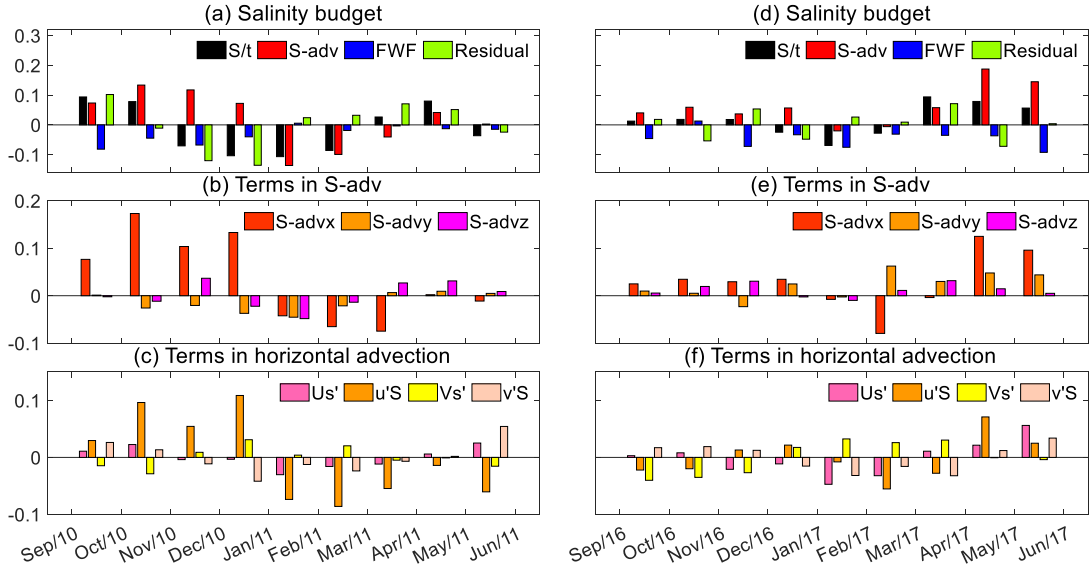


Figure 13. Time series of the averaged anomaly of different budget components (Unit: psu per month) during (a-c) 10A11S and (d-f) 16A17S based on ECMWF ORAS5 salinity data in the main high salinity area. S/t, S-adv, FWF in (a) and (d) represent the salinity anomaly tendency, horizontal advection plus vertical entrainment terms and surface FWF term, respectively. The residual term ϵ includes the horizontal and vertical mixing, and the accumulation of errors from the other terms. S-advx, S-advy and S-advz in (b) and (e) represent zonal horizontal advection, meridional horizontal advection and vertical entrainment terms, respectively. Us' , $u'S$, $u's'$, Vs' , $v'S$ and $v's'$ in (c) and (f) represent $-\bar{u} \frac{\partial [s]'}{\partial x}$, $-u' \frac{\partial [\bar{s}]}{\partial x}$, $-u' \frac{\partial [s]'}{\partial x}$, $-\bar{v} \frac{\partial [s]'}{\partial y}$, $-v' \frac{\partial [\bar{s}]}{\partial y}$ and $-v' \frac{\partial [s]'}{\partial y}$, respectively.

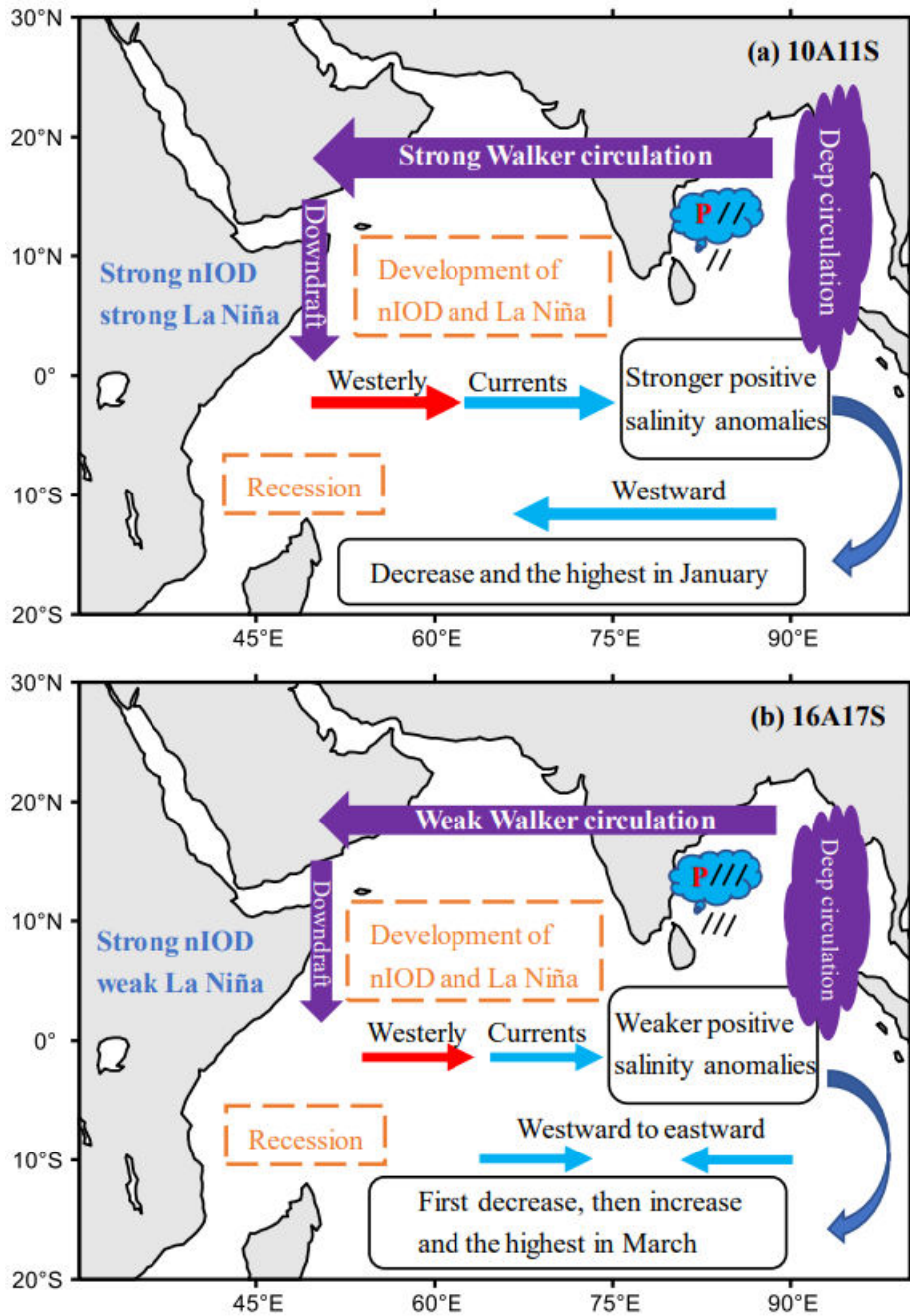


Figure 14. Schematic diagrams of the key processes influencing the extremely high salinity anomalies during (a) 10A11S and (b) 16A17S. The red (blue) arrows indicate the wind (current) fields. The purple arrows indicate atmospheric circulation and red 'P' means the precipitation.